DOCTORAL THESIS

Three-Dimensional Image Processing for Artifact Reduction and Quality Improvement in Medical X-ray Computed Tomography

(医療用 X 線 CT 画像におけるアーチファクト除去および画質向上のための 3 次元画像処理)

KITAMI INSTITUTE OF TECHNOLOGY

DOCTORAL COURSE OF MEDICAL ENGINEERING

DONG JIAN

(董　建)

September, 2014

Contents

Chapter I Introduction

1.1 Medical imaging

Medical imaging is a discipline within the medical field which involves the use of technology to take images of the inside of the human body. These images are used in diagnostics and in routine healthcare for a variety of clinical situations. Medical imaging is always referred to for clinical decision making, because it is frequently used to help doctors reach a correct diagnosis, and there are a number of different types of technology used in medical imaging.

The goal of medical imaging is to provide the information of the inside of the body in a way which is as non-invasive as possible. An imaging study can be used to identify abnormal physical conditions, such as bone fractures, benign and malignant, tumors, leaking blood vessels, cardiovascular diseases, and so forth. One of the most frequently used diagnostic imaging is the X-ray examination.

X-ray computed tomography (CT) examination is the cross-sectional imaging using X-ray [1]. It is also possible to use ultrasound to look inside the body by bouncing sound waves from the body surface to make cross-sectional images. To utilize magnetic resonance imaging is to clarify the cellular status of hydrogen and water. In addition to statistic images, medical imaging can also produce dynamic images, such as scans of brain activity or pictures of the heart in motion that can be used to look for cardiovascular diagnostic issues. The endoscopic viewing is slight invasive techniques which involve the insertion of a camera into the body to take video of an area of interest.

Some imaging studies simply require a capture of an image, while others involve the introduction of a contrast material to the body. Contrast materials are swallowed or injected, and they are designed to be highly visible in the image,

allowing clinicians to follow their shadow through the body. A barium swallow, for example, is used in an X-ray examination of the digestive tract to look for ulcers and perforations, while radioactive contrasts may be injected to look for signs of malignant tumors. Iodinated contrast media is also used for various diagnostic purposes.

1.2 X-ray Computed Tomography

Here, I am going to highlight the technology of computed tomography used in medical imaging. X-ray CT is a technology to produce tomographic images (virtual slices) of specific areas of the scanned object, allowing the user to see what is inside it without cutting it open. Cross-sectional images are used for diagnostic and therapeutic purposes in various medical disciplines [1]. As X-ray CT is the most common form of CT in medicine and various other contexts, the term, CT alone, is often used to refer to X-ray CT, although other types exist, such as positron emission tomography (PET) and single-photon emission computed tomography (SPECT).

A CT image is typically called a slice, as it corresponds to what the object being scanned would look like if it were sliced open along a plane. A CT slice corresponds to a certain thickness of the object being scanned. The gray levels in a CT slice image correspond to X-ray attenuation, which reflects the proportion of X-rays scattered or absorbed as they pass through the object being scanned. X-ray attenuation is primarily a function of X-ray energy and the density and composition of the material being imaged [2]. The CT number differs largely in a CT slice when different tissues have different X-ray attenuations. The measurement unit of CT number is Hounsfield-Unit (HU). The HU scale is a linear transformation of the linear attenuation coefficient measurement into one in which

the radio-density of distilled water (at standard pressure and temperature) is defined as 0 HU. And value of different tissues is described in Table 1.1. The HU scale applies to medical grade CT scans but not to cone beam CT scans. The HU scales in Table 1.1 were referenced from Wikipedia (Accessed at June, 2014. http://en.wikipedia.org/wiki/Hounsfield_scale).

Table 1.1. HU scale of different tissues or materials

Material	HU value	Notes
Air	-1000	vacuum as well, for all practical effects
Fat	-100 to -50	
Water	0	Distilled, at room temp and 1 atm
Muscle	+10 to +40	
Blood	+30 to +45	
Bone	+700 to +3000	+700 (cancellous bone) to +3000 (dense bone)

Since normal tissues and lesioned parts have different X-ray attenuations, the value scale is usually between -1000 HU and +3000 HU. Practically, human eyes have a relatively limited capability of resolution, so window width (WW) and widow level (WL) should be set suitable in order to get the optimal display when observing the details of certain tissue or lesioned part [3].

Of all the internal imaging procedures available to physicians, the CT scan is the most detailed, and can give a clinician the most complete picture of what's happening inside a patient's body. They are particularly useful and widely used in diagnosing benign and malignant lesions, and it can help physicians in planning subsequent procedures such as a biopsy, surgery, radiotherapy or other treatments with high precision. The CT scan procedure is noninvasive and painless, and is generally quick and convenient for most patients. It's widely available at a range

of different treatment centers [1, 4].

However, there are some disadvantages of CT examinations. Compared to other diagnostic modalities, CT scans deliver relatively high radiation doses to patient [2, 3]. While this is not usually a problem for a single scan, patients who need to undergo repeated examinations can be subjected to a significant level of radiation, increasing their cancer risk. What's more, some contrast materials are sometimes needed in CT scans in order to obtain a clear view of specific organ or vessels. Some people can have an allergic reaction to this, and symptoms can include a metallic taste in the mouth, itchiness, hives and shortness of breath.

1.3 Artifacts

Although images produced by CT are generally faithful representations of the scanned volume, the technique is susceptible to a number of artifacts [5].

a.) Motion artifact

This is seen as blurring and/or streaking, which is caused by movement of the object being imaged or heart beating. A better way to reduce object movement is to require cooperation of patients, while it is futile for heart beating artifact.

b.) Ring artifact

This is probably the most common mechanical artifact. There are usually one or many "rings" appear within an image. It is usually due to a detector fault, namely function fail occurs of a specific detector. The strategy of ring artifact reducing is to repair or change the broken detector.

c.) Metal induced artifact

When utilizing computed tomography scans, clinicians are often challenged by image distortions caused by high atomic-number and high-density metallic bio-materials such as prosthesis, screws or dental fillings [6, 7]. The metals often have

a high X-ray absorption coefficient, which causes an inaccurate value outputted on the detector [8]. Metals often cause streak-like artifacts in CT scans, making it difficult for clinicians to clearly delineate between lesions and healthy tissues.

Similar artifacts are also observed by the presence of other metallic biomaterials. Usually the streak artifacts caused by metallic materials on multi-detector row CT (MDCT) images are intense radial rays [9-11]. Metallic biomaterials that are not only in the oral and maxillofacial region but also in other body regions cause the lack of projection data owing to extremely high X-ray absorption coefficients. Resulting sonogram (another name of projection data) patterns show the corruption by such missing data [12, 13].

The traditional CT reconstruction method, filtered back-projection (FBP) algorithm, is the standard procedure on almost all modern CT systems in clinics. But it cannot deal with such metal-induced inconsistencies [4]. Fourier transform was carried out to the sonogram of the object. Then filter was utilized to block some high frequency signal. After inverse Fourier transform and back projection, the object was reconstructed. However, the method often bring some image blurring problems. Some kinds of algorithms, subsequently, have been proposed for metal-induced streak artifact reduction. They usually take methods in which the partly corrupted sonogram data are repaired by either the replacement of intact data or the relevant interpolation [14-16].

1.4 Purpose of this study

CT images of the dento-alveolar region are sometimes rendered unusable for diagnostic purposes because of the appearance of streak artifacts that are often caused by the presence of metallic prosthetic appliances. On the other hand, because of advances in hardware and software in CT systems, and clinical needs,

CT examination with thin slice thickness is routinely carried out in the dento-alveolar region and other head and body regions.

We found that an artifact-free/intact slice depicted very similar anatomical structures to the adjacent slices that contained streak artifacts. We first proposed iterative correction to an image with heavy streak artifacts using the artifact-free neighboring slice for the metal-induced streak artifact reduction. Here, the maximum likelihood-expectation maximization (ML-EM) reconstruction algorithm realized the iterative correction. To improve reproducibility of anatomical structure, successive iterative reconstruction method was proposed subsequently. In addition, the ordered subset-expectation maximization (OS-EM) reconstruction algorithm was applied to reduce the calculation time on the procedure of streak artifact reduction. Moreover, the effects of the small region of interest (ROI) setting and fast calculation by the compute unified device architecture (CUDA) programming optimized for the general-purpose graphic processing unit (GPGPU) were investigated.

After streak artifact was reduced on CT slices, 3D filtering methods and the corresponding 2D filters were examined to improve both image quality and the precision of tissue depiction. Region growing method was utilized for tissue segmentation.

In general, the objective of this research work was to reduce the metal-induced streak artifacts using successive iterative reconstruction method, ML-EM and OS-EM algorithm. And to improve image quality of cone beam CT (CBCT) images by using 3D filtering method and region growing method.

Chapter II Format and display of medical image

2.1 DICOM image

DICOM (Digital Imaging and Communications in Medicine) is the standard of digital imaging and communication in medicine area. It was established by DICOM standardization committee. DICOM supporting devices makes it possible for data transfer between multi-modalities from different manufactures. The DICOM image is different from other standardized image formats (JPEG, BMP, TIFF, GIF, etc.). It contains special information about patient and examination, etc.

DICOM image file is usually composed of multiple data elements (Fig.2.1). In each data element, there are tag (group number and element number), value representations (VR), data length and data itself.

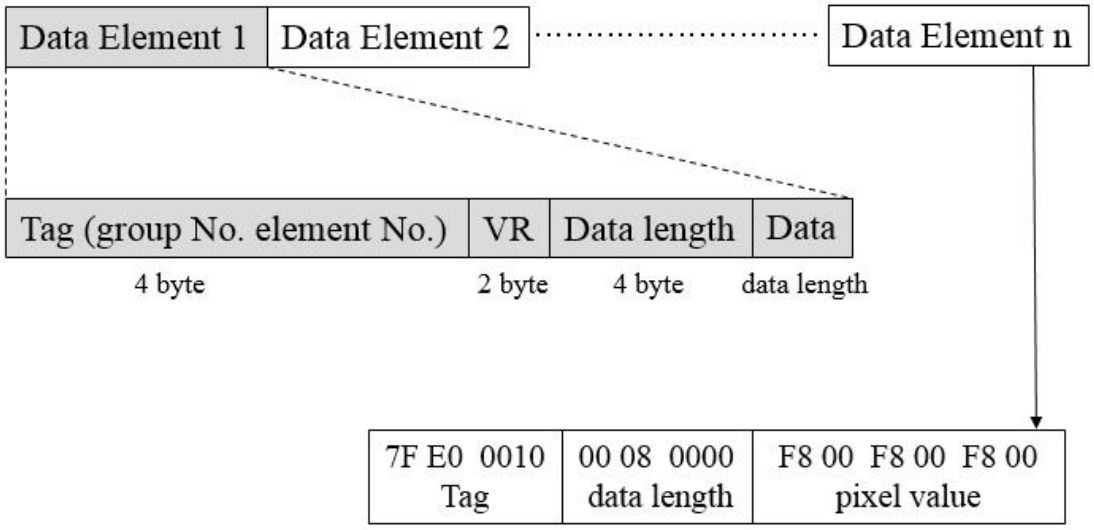

Fig.2.1.The composition of DICOM image format

To read out the DICOM image data correctly, it is necessary to get information about image rows, image columns, bits of per pixel and starting point of image data. The information descripted above is located in different elements. Usually, the tag for image rows is 0028 0010. The tag for image columns is 0028 0011. The tag for pixel bits allocated is 0028 0100. And the tag for image data information is 7FE0

1000. In Fig.2.1, the last element is image data element whose tag is 7FE0 1000. In this element, value representations part is omitted. The data length can be calculated as 0008 0000=2^{19} (512 x 512 x 2 byte) and a pixel value can be calculated as F800=1111 1000 0000 0000= -2048.

Fig.2.2 shows only a part of DICOM image information. The original DICOM image is a MDCT slice with 512 x 512 pixels. Besides the circled basic information, pixel spacing, window center and window width are provided.

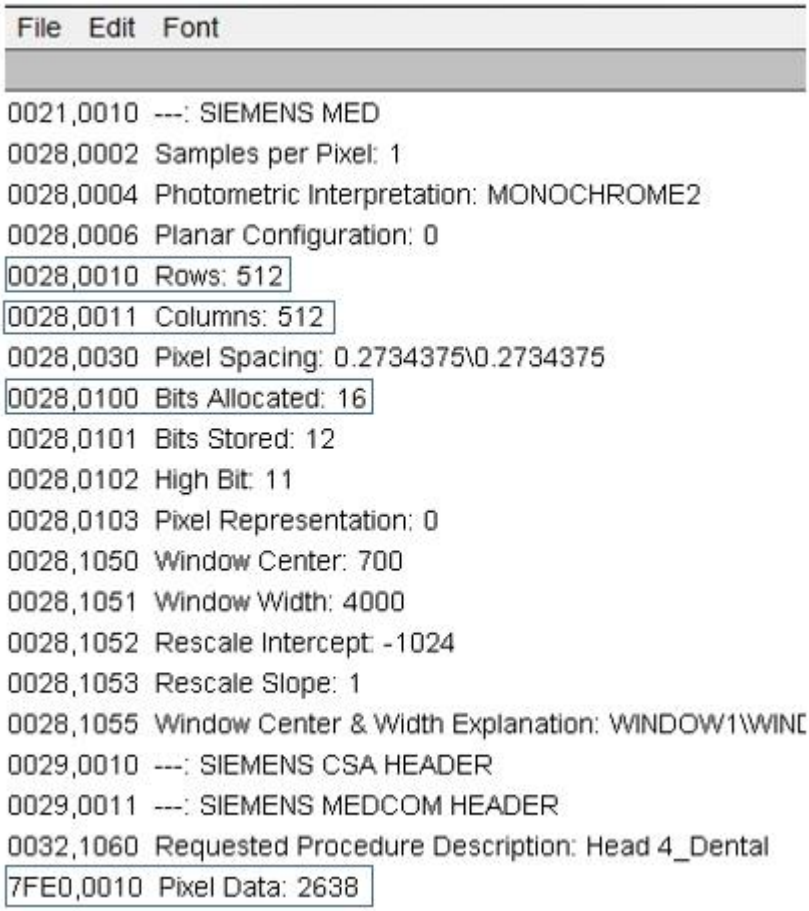

Fig.2.2. A part of DICOM image information originated from a MDCT slice

2.2 Software for medical image displaying

An image displaying software is indispensable in medical image processing area. In this study, two image displaying and processing software were used. They are

Image J (Ver.1.421, NIH) and OsiriX (Ver.4.1.2, OsiriX Fundation, Geneva, Switzerland).

2.2.1 Image J

Image J is written in Java, which allows it to run on Linux, Mac OS X and Windows, in both 32-bit and 64-bit modes. Image J and its Java source code are freely available. Fig.2.3 shows the main interface of Image J.

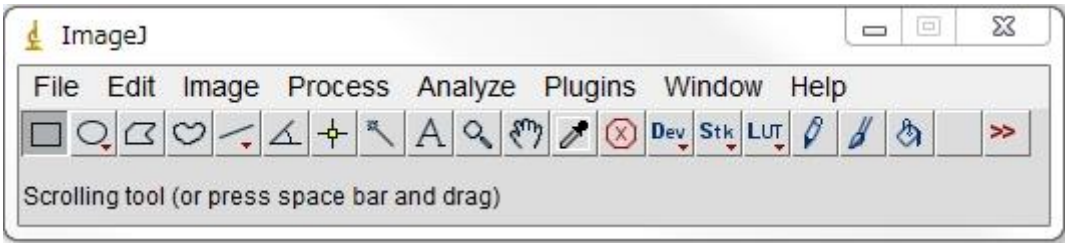

Fig.2.3 Main interface (main bar) of Image J.

In image processing area, it is very common to open a raw image data. Push 'File' button, select 'Import', 'Raw…' in the drop-down menu, and then select the raw image data according to its document path. Fig.2.4 shows an example to open a raw data with 16-bit per pixel, 512 x 512 pixels. Images are often converted to different formats. Appropriate parameters are required to open the image data correctly by Image J. To verify pixel's bits allocate is required in some cases and the premise is that data size, rows, and columns are known. Usually, the size of a16-bit/pixel CT image with 512 x 512 pixels is 512kB. If a raw data (CT image) is 1024kB, the bits allocate can be calculated as 32-bit and the image can be concluded as a float format data.

Image J can calculate area and pixel value statistics of user-defined selections and intensity thresholded objects. It can measure distances and angles. It can create density histograms and line profile plots. Also it supports standard image

processing functions such as logical and arithmetical operations between images, contrast manipulation, convolution, Fourier analysis, sharpening, smoothing, edge detection and median filtering. It does geometric transformations such as scaling, rotation and flips. The program supports any number of images simultaneously, limited only by available memory.

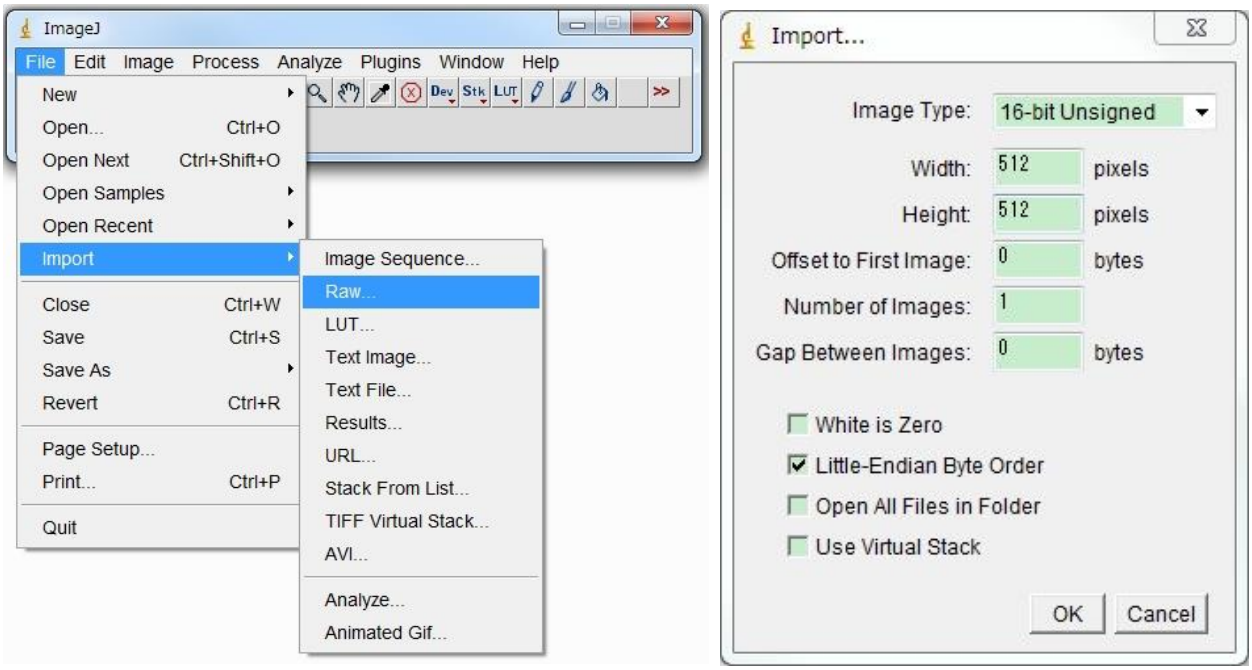

Fig.2.4. An example to open a raw data with 16-bit per pixel, 512 x 512 pixels

2.2.2 OsiriX

OsiriX is an image processing application for Mac dedicated to DICOM image produced by medical equipment. It can also read many other file formats: TIFF (8, 16, 32 bits), JPEG, PDF, AVI, MPEG and QuickTime [16].

OsiriX has been specifically designed for navigation and visualization of multimodality and multidimensional images: 2D Viewer, 3D Viewer, 4D Viewer (3D series with temporal dimension, for example: Cardiac-CT). The 3D Viewer offers all modern rendering modes: multi-planar reconstruction (MPR), surface rendering, volume rendering and maximum intensity projection (MIP). OsiriX is released under a free software license and runs under Mac OS X [17].

In this study, OsiriX (Ver. 4.1.2, OsiriX Fundation, Geneva, Switzerland) was used to show volume rendering of dento-alveolar region. Images before and after streak artifact reduction were compared. Subsequently, MPR images were produced by OsiriX for viewing image quality improvement.

Chapter III Image reconstruction algorithms

3.1 Projection data acquisition

In X-ray CT equipment, X-ray traverses the scanned object and attenuated X-ray is collected by detector. The data set from detector is projection data. Then the projection data is sent to computer for image reconstruction, and tomographic images can be obtained shortly [18-22]. In this study, we developed a projection data acquisition algorithm to carry out image reconstruction instead of using the original projection data from CT modality. The projection data here is calculated based on CT image.

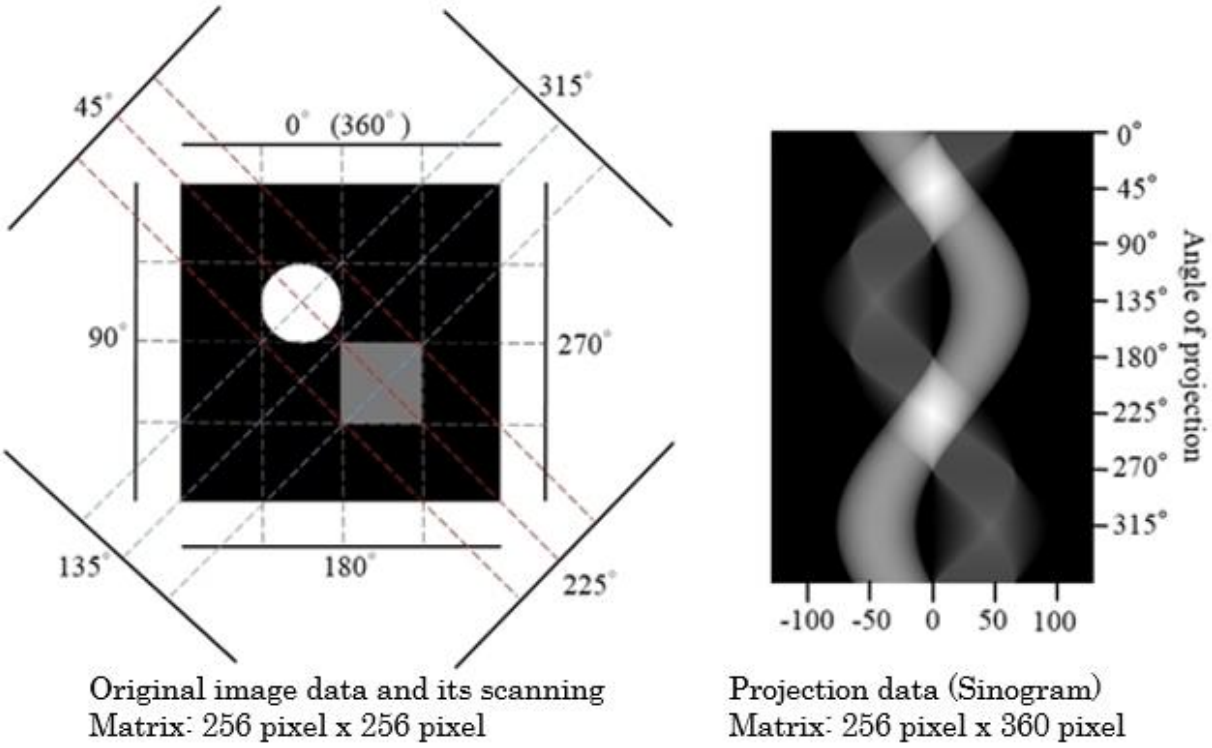

Fig.3.1 Example of computing a 256 x 256 matrix image's projection data. Each row in the projection data represents the detected value of the detector for a designated angle. The projection data was acquired in 360 directions with 1° intervals, thus the pixel matrix was 256 x 360.

Each pixel of the image has a CT number, which is proportional to x-ray transparency. When the x-ray traverses each pixel, the shape of each pixel is usually a trapezoid, depending on the angle between the projection and each pixel

square. In special cases, projection shapes of square pixels become either a square at 0°, 90°, 180°, and 270° or a triangle at 45°, 135°, 225°, and 315° when the coordinate axes are set along edges of the image (Fig.3.1). The image matrix contained 256 x 256 pixels. During the projection data calculation, the value is accumulated by adding the respective pixels' CT number. If the shape of the projection is not square, the detectability will be divided by the center of the detector element and neighboring elements [18-22]. The projection data were acquired in 360 directions with 1 degree intervals, and the projection data's pixel number was 256 x 360 in Fig.3.1.

3.2 Maximum likelihood-expectation maximization algorithm

As the iterative restoration methods, we used two algorithms; namely, ML-EM algorithm and OS-EM algorithm. The ML-EM algorithm results in an approximation between the processing image and the target image [18-24]. The formulation of ML-EM algorithm is described as follows:

$$\lambda_j^{(k+1)} = \frac{\lambda_j^{(k)}}{\sum_{i=1}^{n} C_{ij}} \sum_{i=1}^{n} \frac{y_i C_{ij}}{\sum_{j'=1}^{m} C_{ij'} \lambda_{j'}^{(k)}}$$

Where λ (Lambda) is the output value of each pixel; k, the counter of iteration (loop variable); j, the number of pixels (1- m), m = 262,144 if the image matrix is 512 x 512; i, the number of detector's element (1 - n); Cij, detecting probability as the relation of pixel (i) and detector's element (j); and yi, the projection data by the pixel (i).

We applied the ML-EM algorithm to reconstruct images following the steps shown in Table 3.1. A target image is needed to reconstruct an assumed initial image (Step 1). Based on the projection data acquisition rules, the projection data of two images can be calculated (Step 2). Then the two projection data sets are

compared pixel by pixel. When the values are different, the pixel value which belongs to projection data of initial image is modified to another value. The new value must be calculated using the value of target image's projection data as a reference (Step 3). After every pixel is compared on the projection data, new projection data are produced. Next, the back projection operation is executed based on the newly produced projection data (Step 4). Then a new image, which contains both features of the target image and initial image, can be obtained (Step 5). More iterative operations will lead to the new image appearing features of the target image dominantly (Step 6). Of these steps, the key procedure is the process of comparing the projection data of target image and the newest image, and then making an approximation between them [18-24]. Fig.3.2 shows the process of image reconstruction from K times to K+1 times.

Table 3.1. Execution steps of maximum likelihood-expectation maximization algorithm

Execution steps	*Procedures*
Step 1	Select a target image and create an initial ("headmost") image
Step 2	Compute projection data of target image.
Step 3	Compute projection data of initial image. Then compare it with projection data of the target image in matrix pixel sequence
Step 4	Reconstruct the assumed image according to the projection data ratio obtained in Step 3
Step 5	Normalize the reconstructed image and set as the new initial ("headmost") image.
Step 6	Repeat Step 3 to Step 5 until achieving the iteration time setting

3.2.1 Matrix reconstruction (3 x 3 pixel) by ML-EM

Based on ML-EM iterative restoration rules, we did a simulation to show image reconstruction process on a 3 x 3 matrix. We first assumed image pixels as 1 to 9 in pixel order. A 3 pixel detector was used and only two detect angles were set (0°

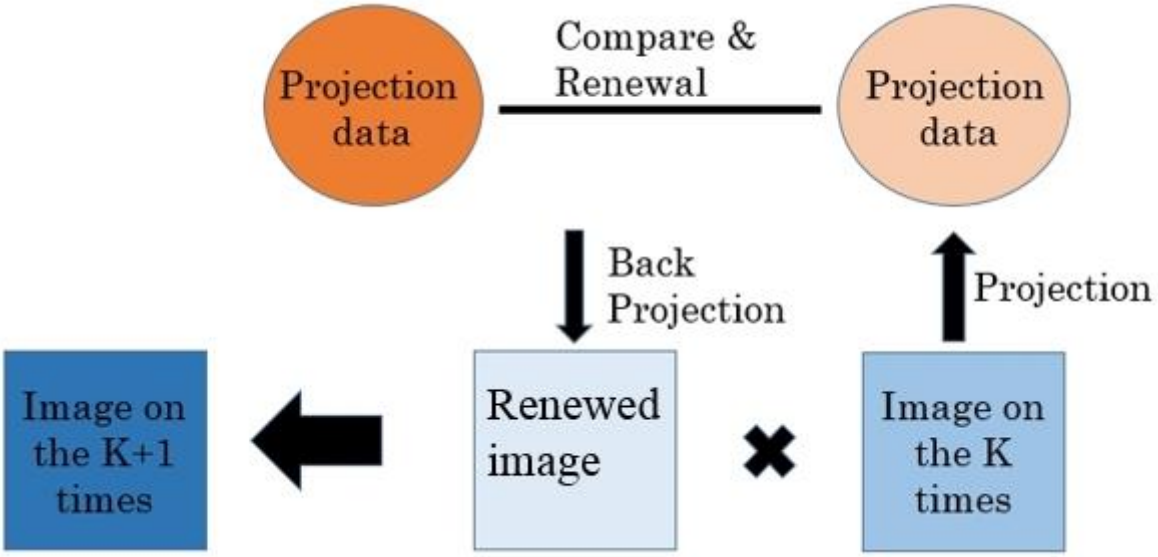

Fig.3.2 Image reconstruction from K times to K+1 times.

and 90°) in this simulation. Namely, the projection data acquisition was carried out on 0°and 90° directions. The target matrix and its detectors are shown in Fig.3.3. The cumulated amount of corresponding pixels was defined as projection pixel data. For example, on 0° detector, pixel data 12 was accumulation of matrix pixels 1, 4 and 7.

For matrix reconstruction, an assumed matrix (initial matrix) was created as all pixels were 1 (Fig.3.4). Projection pixel data can be calculated easily as 3. Since they were different from the target image' projection data, reconstruction process

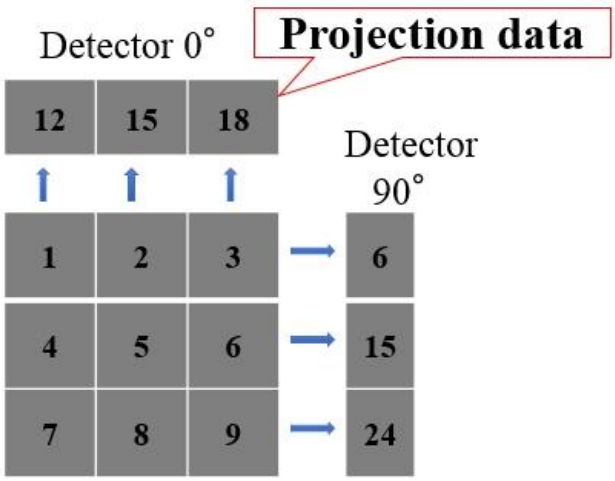

Fig. 3.3. Target matrix and its projection data.

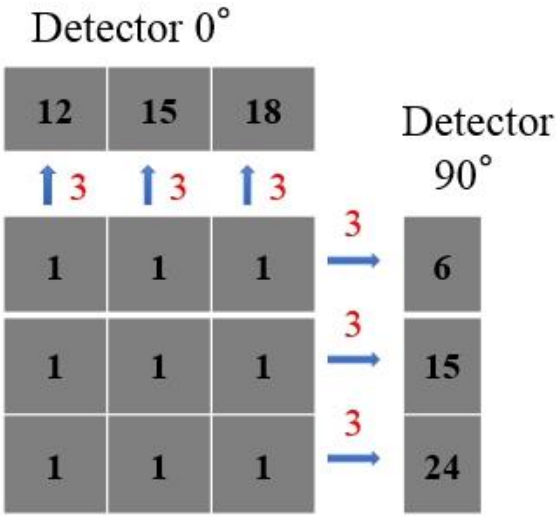

Fig.3.4. Assumed initial matrix.

was necessary. Each matrix pixel was calculated based on the formula of ML-EM algorithm. The 1st pixel and the 5th pixel calculation were carried out as follows:

$$\lambda_1^1 = \frac{1}{1+1}\left(\frac{12\times1}{1\times1+1\times1+1\times1}+\frac{6\times1}{1\times1+1\times1+1\times1}\right) = 3$$

$$\lambda_5^1 = \frac{1}{1+1}\left(\frac{15\times1}{1\times1+1\times1+1\times1}+\frac{15\times1}{1\times1+1\times1+1\times1}\right) = 5$$

Other pixels were calculated in the same way. The reconstructed matrix can be obtained (Fig.3.5). Pixel number changed largely. However, the pixels were different from that on the target matrix. Another reconstruction process was needed.

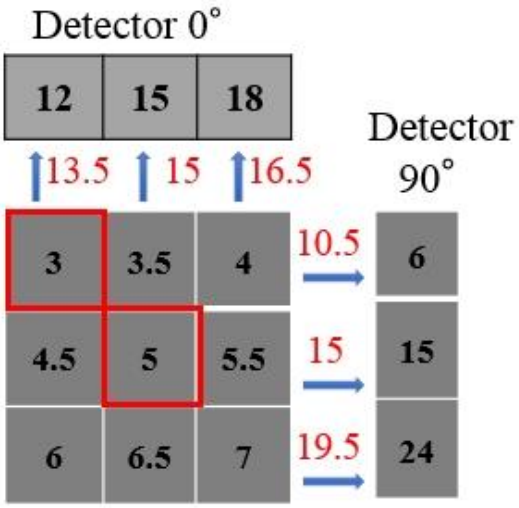

Fig.3.5 The reconstructed matrix on the first time iteration.

The second time iteration was carried out similarly as the first time iteration. Also the first and the fifth pixels were calculated as samples. The calculations were shown below:

$$\lambda_1^2 = \frac{3}{1+1}\left(\frac{12\times1}{3\times1+4.5\times1+6\times1}+\frac{6\times1}{3\times1+3.5\times1+4\times1}\right) = 2.19$$

$$\lambda_5^2 = \frac{5}{1+1}\left(\frac{15\times1}{3.5\times1+5\times1+6.5\times1}+\frac{15\times1}{4.5\times1+5\times1+5.5\times1}\right) = 5$$

Each pixel data was updated due to the reconstruction. New obtained matrix is shown as Fig.3.6. The pixel numbers were still different from the target matrix and the next reconstruction process was verified to be needed.

2.19	2.75	3.32
4.25	5	5.75
6.36	7.25	8.13

Fig.3.6 The reconstructed matrix on the second time iteration.

Similar matrix reconstructions were carried out for dozens of times. It had a trend that pixel numbers approximated the target matrix little by little. Fig.3.7 shows the 26th reconstructed matrix. Pixel numbers were not all the same with the target matrix, but the calculated projection data were identical. By performing round-up (omitting decimal fractions smaller than 0.5 and counting all others) to the pixel numbers, the target matrix can be obtained. Here, it can be decided that the matrix has been reconstructed to the target matrix until 26th restoration.

In this simulation, the target matrix only has 3 x 3 pixels and furthermore, only 2 detector directions were set as 0° and 90°. Although the uncomplicated model can be reconstructed on the 26th iteration, much more iterations could be speculated

to be needed if the matrix or image is a larger one [19].

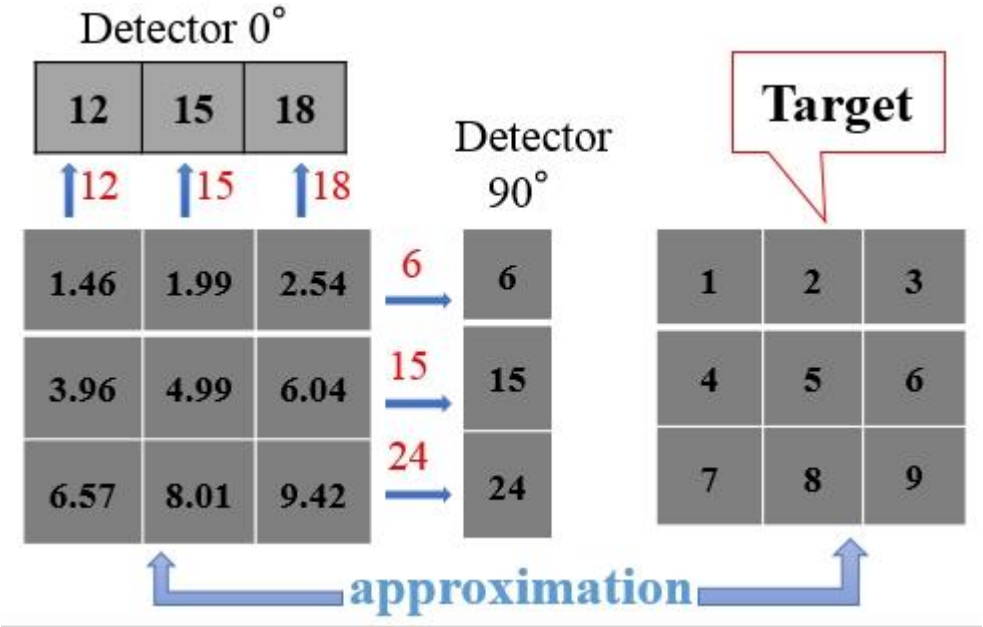

Fig.3.7 The 26th iteration of the matrix. Target matrix is reconstructed here.

3.2.2 Convergence validation of ML-EM on practical image.

We performed a practical image reconstruction following ML-EM algorithm. An image containing a circle and a square was set to be the target image. Its matrix is 256 x 256 pixels, 32-bit per pixel and the size of the image is 256kB.

Pixel value on the circle part is 85.0 and it is 40.0 on the square part. The pixel value on the background is 0.0. Based on the projection data acquisition rule, projection was carried out 360 directions with 1° interval. The target image and its projection data is shown in Fig.3.8. The image used here is the same with Fig.3.1. Usually the projection data of a practical image is symmetrical on both left-right and up-down.

The initial image was created to be a black and white stripe image whose matrix is also 256 x 256 (Fig.3.9). Bits location on each pixel is 32-bit, and the image size is 256 kB. Pixel value on the white part is 80.0 and it is 40.0 on the black part. Usually pixel value of initial image can be decided freely, but 0 should be except.

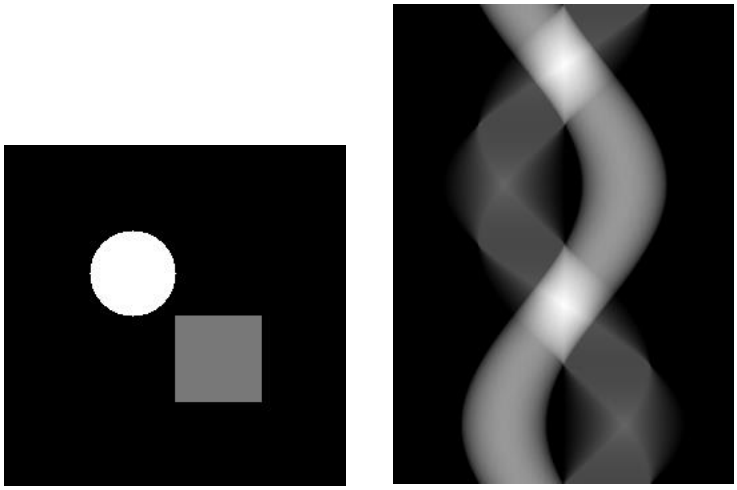

Fig.3.8 The target image (256 x 256) and its projection data (256 x 360).

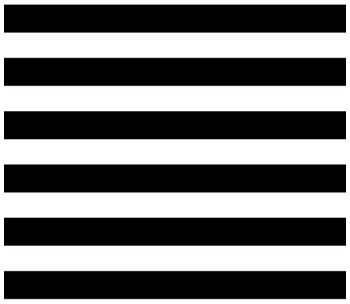

Fig.3.9 The initial image (256 x 256).

Iterative restoration ML-EM program was carried out for 300 times. The projection data from Fig.3.8 and the stripe image from Fig.3.9 were used as input images. Output images at different iteration times are shown in Fig.3.10. They are the processed images at the 1st, 2nd, 3rd, 4th, 5th, 10th, 20th, 30th, 40th, 50th, 100th, 150th, 200th, 250th, and 300th (Fig.3.10a~o) iteration times respectively.

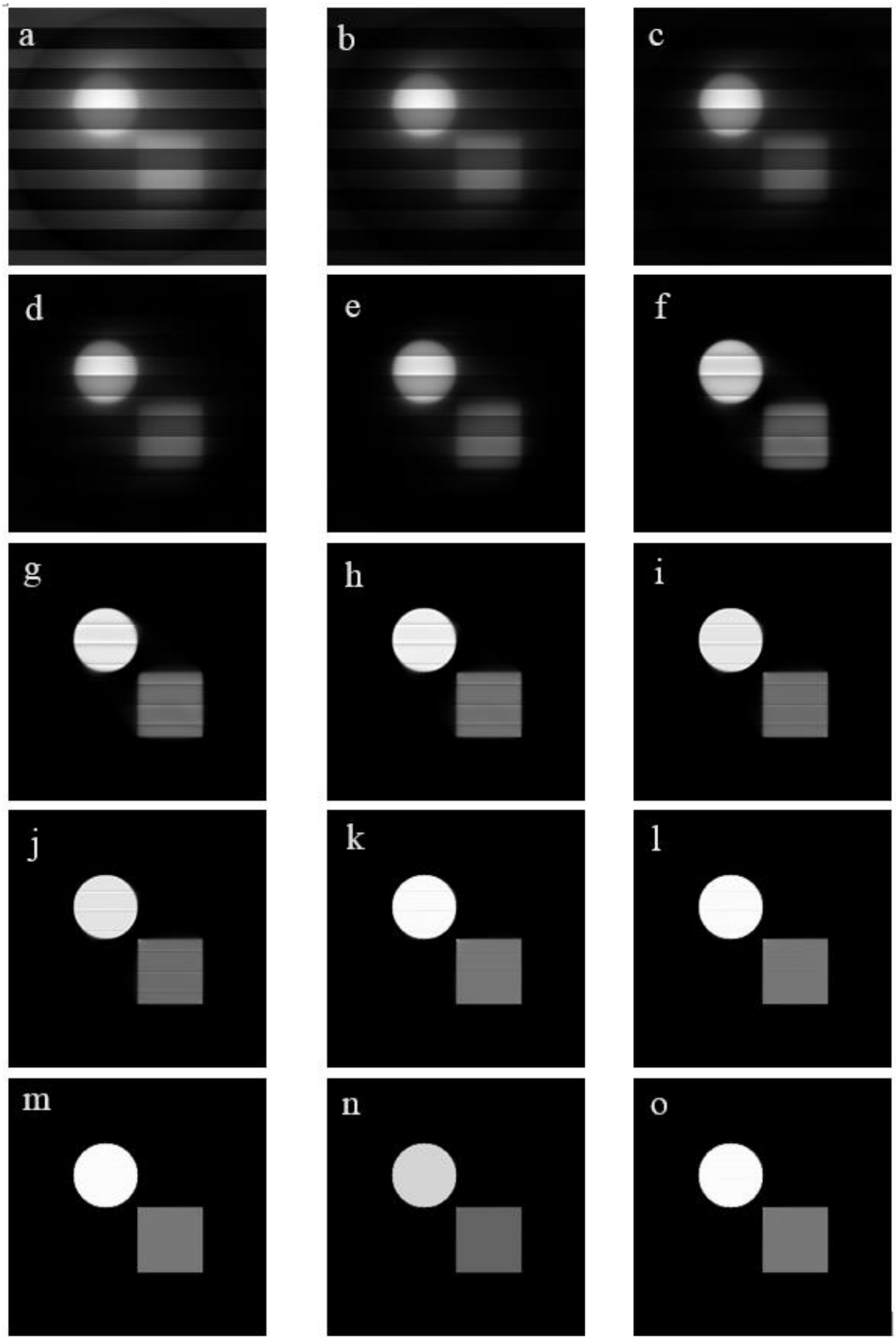

Fig.3.10. Iterative corrected images by ML-EM algorithm at the 1st, 2nd, 3rd, 4th, 5th, 10th, 20th, 30th, 40th, 50th, 100th, 150th, 200th, 250th, and 300th iteration (a~o) respectively.

The inputted stripe image was iteratively corrected using target image's projection data. ML-EM restoration program was carried out for 300 times. At the initial stage, image density of the 1st iteration changed heavily. Both white and black density attenuated to a large extent. Importantly, the circle and square geometry occurred at the right position although they were blurred. It can be concluded that the target image's projection data corrected the initial image heavily at the 1st iteration. The processed image at the 2nd iteration is shown in Fig.3.10b. Black-white stripe disappeared at the image periphery. The visibility of circle and square shape increased. The 3rd iteration image is shown in Fig.3.10c. Black-white stripe remained only at the center part of the image and the shape of circle and square became sharp gradually. As the iteration times increased, features of the target image were enhanced dominantly. On the contrary, the features of the initial stripe image were reduced step by step. The processed image at the 300th iteration clearly presented the target image characters. Almost identical circle and square to that in target image were depicted at 300th iteration.

Next, the image convergence analysis is carried out on pixel value aspect. Several selected coordinate pixels from images on different iterations were compared in Table 3.2.

Table 3.2 Pixel values of five selected coordinate pixels from different iterations.

Pixel value	P(28,30)	P(70,70)	P(95,95)	P(128,128)	P(158,158)
Initial image	40.0	40.0	80.0	80.0	40.0
1st	3.5022	7.4912	28.3545	16.5634	9.1795
2nd	1.9219	9.0581	58.8809	19.9661	14.4060
3rd	0.8214	8.7302	86.2047	17.5073	19.5227
4th	0.2990	7.2806	100.1103	13.1634	23.9786
5th	0.1004	5.6356	103.8053	9.1632	27.4193

10th	3.1092	1.0825	92.9323	1.3473	33.5859
20th	2.3798	0.0275	85.3993	0.1282	36.5086
30th	1.8353	6.9881	84.4911	0.1742	38.2969
40th	1.4775E-19	1.8486E-5	84.3103	1.4003	39.2439
50th	1.2315E-24	5.0333E-7	84.3193	7.6368	39.7339
100th	0.0	9.500E-15	84.6235	33.2671	40.0510
150th	0.0	2.2081E-22	84.6719	36.0063	39.7824
200th	0.0	5.7919E-30	84.6970	36.5632	39.9621
250th	0.0	1.6521E-37	84.7736	36.7606	39.5395
290th	0.0	1.6E-43	84.8658	36.8771	39.5285
300th	0.0	5.6E-45	84.8918	36.9057	39.5299
Target image	0.0	0.0	85.0	40.0	40.0

In Table 3.2, pixel values of five selected coordinate pixels from different iterations were compared. As iteration times increased, pixel values on corresponding coordinate more and more approximated the pixel value in target image. The pixel values in 300th iteration were almost the same with that of target image. It can be concluded that the target image was reconstructed by 300 iterations.

The execution time for 300 times iteration of ML-EM program was 7 min 5 sec. The desktop personal computer that we used had an Intel(R) Core(TM) i7-3770K central processing unit, running at 3.50GHz and 3.50GHz. The RAM memory was 32 GB. Windows 7 Enterprise operating system was installed with 64 bit version.

3.3 Ordered subset-expectation maximization algorithm

OS-EM algorithm is also used as iterative restoration on image reconstruction. OS-EM algorithm which is based on ML-EM algorithm divides the projection data to several subsets and carries out projection, projection data comparison, image renewal and back projection to just the data belonged to the given subset [21, 22, 25-28].

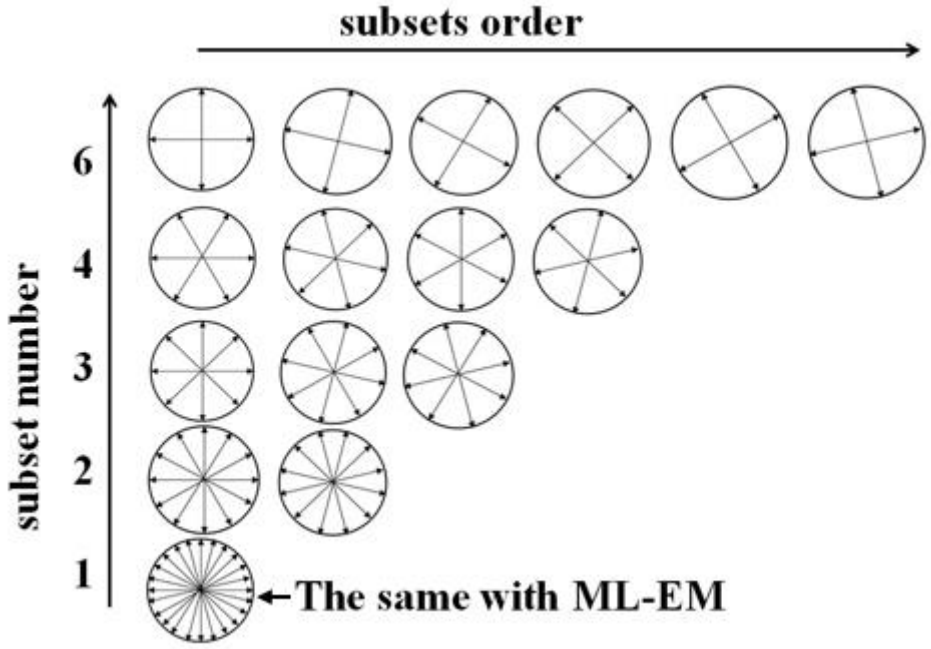

Fig.3.11 The OS-EM subsets combination. An example of 24 projection direction.

Subsets of 24 projection angle examples are schematically shown in Fig.3.11. The 24 projection angles can be divided into {1, 2, 3, 4, or 6} subsets as shown in Fig.3.11. For the OS-EM algorithm, the image quality factor, namely the image update number, is the product of subset numbers and iteration times.

Image update number = subset number × iteration times

Therefore, there will be more image updates during one time iteration and as a result, images can be reconstructed quickly. Thus, the OS-EM algorithm is considered to be the solution for fast image reconstruction [18, 21, 22, 25, 27].

The execution sequence of OS-EM algorithm is shown below:

1. Calculate and determine the detection probability.
2. Input the target image's projection data and create the initial image.
3. Compute projection data of initial image only on angles belongs to special subset.
4. Compare the obtained projection data from step 3 with target image's projection of special subset.
5. Do back projection based on the special subset projection ratio got from step 4.

6. Normalize the back projected image and multiply it to initial image.

7. Do the same procedures to other subsets.

8. Set the newly reconstructed image as new initial image. Execute the same procedures for iteration times.

In OS-EM algorithm, if we set subset number as 1, the program procedure will be the same with that of ML-EM algorithm.

3.3.1 Convergence validation of OS-EM on practical image

In this section, we performed a practical image reconstruction following OS-EM algorithm. The same target image and initial image were selected with that in section 3.2.2. The target image and its projection data is shown in Fig.3.8, and the initial image is shown in Fig.3.9.

We set the OS-EM parameters as subset number = 8, iteration times=50. The projection data from Fig.3.8 and the stripe image from Fig.3.9 were used as input images. Output images at different iteration times are shown in Fig.3.12. They are the processed images at the 1st, 2nd, 3rd, 4th, 5th, 10th, 20th, 30th, 40th, and 50th (Fig.3.12a~j) iteration times respectively.

The inputted stripe image was iteratively corrected using target image's projection data. OS-EM restoration program was carried out for 50 times, and subset number was set to 8. Program was executed on the same desktop computer with that of section 3.2.2. The time consumed for 50 iterations was 1 min 55 sec.

Different results were got from that of ML-EM algorithm. The reconstructed image at the 1st iteration already presented clear background. The black-white stripe shape disappeared completely. At this stage, the shape of circle and square was blurred. The image at the 2nd iteration had a clearer and more intact shape of circle and square. As iteration times increased, the intensity on the circle and

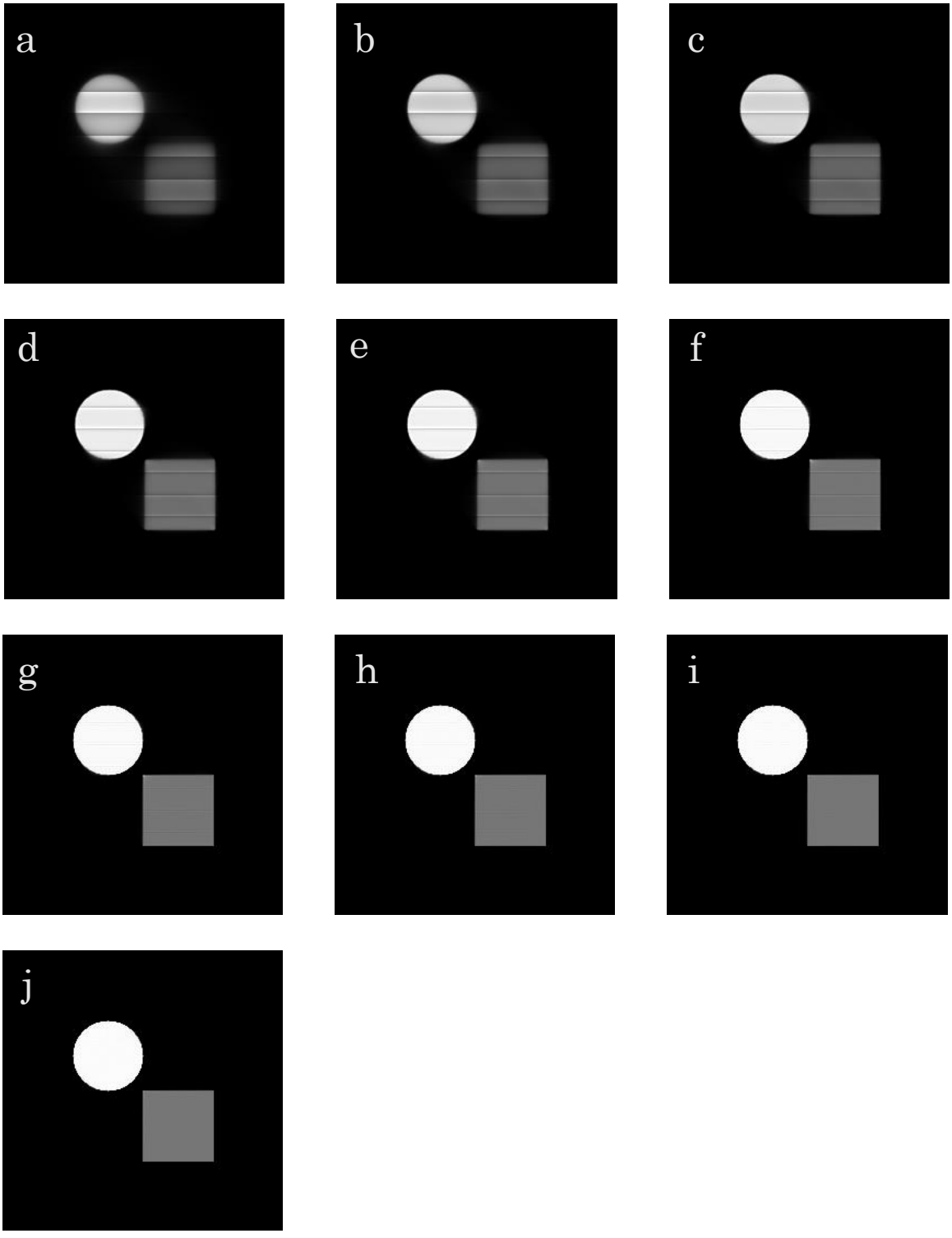

Fig.3.12. Iterative corrected images by OS-EM algorithm at the 1st iteration (a), 2nd iteration (b), 3rd iteration (c), 4th iteration (d), 5th iteration (e), 10th iteration (f), 20th iteration (g), 30th iteration (h), 40th iteration (i), and 50th iteration (j) respectively. Subset number was set to be 8.

square parts approximated that of target image. Stripe pattern became nearly invisible on the 30th iteration image. By intuitive judgment, the image at 40th iteration had the same effect with that of the 300th iteration image by ML-EM.

Table 3.3 Pixel values of five selected coordinate pixels from different iterations

Pixel value	P(28, 30)	P(70, 70)	P(95, 95)	P(128, 128)	P(158, 158)
Initial image	40.0	40.0	80.0	80.0	40.0
1st	0.0030	2.1882	97.5263	2.8075	32.3014
2nd	2.3752E-7	0.1215	86.6501	0.2407	35.4295
3rd	1.7792E-11	0.0063	84.8432	0.1058	37.2907
4th	1.3654E-15	3.3801E-4	84.4218	0.2459	38.4870
5th	1.0779E-19	1.8476E-5	84.3050	1.4092	39.1991
10th	4.2351E-40	1.1144E-11	84.5394	29.0505	40.0839
20th	0.0	6.4962E-24	84.6841	36.1470	39.7210
30th	0.0	5.1060E-36	84.7671	36.7099	39.5338
40th	0.0	1.4E-45	84.961	36.9536	39.5248
50th	0.0	1.4E-45	85.1959	37.1933	39.5795
Target image	0.0	0.0	85.0	40.0	40.0

The image convergence analysis is carried out on pixel value aspect. 5 selected coordinate pixels from images on different iterations were compared in Table 3.3. The same tendency was presented with that in ML-EM iterations. As iteration times increased, the pixel values more and more approximated the corresponding target image' pixel values. The difference from ML-EM iterations was that the pixels values got close to target value perfectly even in the initial stage, such as the 1st iteration or the 2nd iteration. It can be found that the pixel values in the 1st iteration could approximately be located between 5th and 10th iteration values. Namely, the effect of one OS-EM iteration was generally the same with the effect of about 8 ML-EM iterations.

The OS-EM algorithm can reconstruct image data faster without image quality

dropped and it is usually used to reduce the calculation time in comparison with the ML-EM algorithm [21, 22]. The OS-EM algorithm is clinically used for positron emission tomography (PET) and single-photon emission computed tomography (SPECT) examinations in nuclear medicine [29].

Chapter IV Iterative restoration algorithms applied to streak artifact reduction in X-ray CT image. Investigate the variable optimization of ML-EM and OS-EM.

4.1 ML-EM variable optimization in streak artifact reduction

Because of advances in hardware and software in CT system, and clinical needs, CT examination with thin slice thickness is routinely carried out in the dento-alveolar region and other head and trunk regions [30-32]. We found that an artifact-free/intact slice depicted very similar anatomical structures to the adjacent slice that contained the heavy metal-induced streak artifact. Because they depicted very similar anatomical structures, they were selected the processing objects. Therefore, we applied the ML-EM reconstruction algorithm to MDCT images [18-20, 22]. After all, the processing was practically an iterative correction. The objective was to apply iterative correction to an image with heavy metal-induced artifacts using the artifact-free neighboring slice for the artifact reduction, and to investigate the optimization about the iteration times of ML-EM algorithm when used in artifact reduction.

MDCT examination of the maxillary sinus and maxilla was carried out using a Somatom ® Plus 4 Volume Zoom (Siemens, Erlangen, Germany). Principal exposure conditions were: 120 kV, 130 effective mAs, and a slice thickness of 0.5 mm. the pixel matrix of each slice was 512 x 512. Severe metal-induced streak artifacts occurred at several tooth crowns in the maxilla, and in addition, the overlapped regions were invisible.

An MDCT image with heavy streak artifacts caused by metallic dental appliances (Fig.4.1) and its adjacent artifact-free MDCT image (Fig.4.2) were selected. There were 7 slices (0.5mm for a single slice) between the two selected images, namely they were 3.5 mm apart. Our trial was to reduce streak artifacts

on the image in Fig.4.1 by using the projection data from the intact image in Fig.4.2.

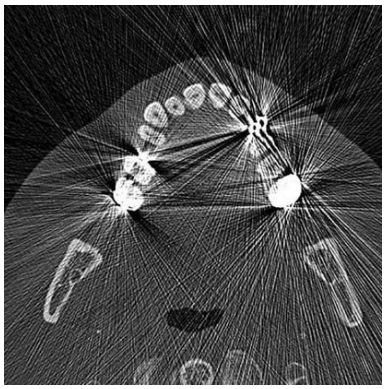

Fig.4.1 An MDCT image with heavy streak artifacts
which are caused by metallic dental appliances.

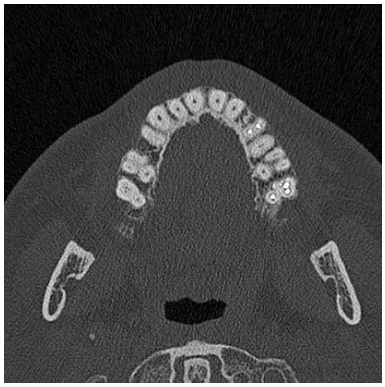

Fig.4.2 An artifact-free MDCT image. This is a neighboring slice (3.5 mm apart) to the slice with heavy streak artifacts shown in Fig.4.1.

Projection data acquisition of the image in Fig.4.2 was carried out based on the rules described in 3.1 section. The projection data is shown in Fig.4.3. Since the projection data were acquired at 360 directions with 1° intervals, the pixel matrix of the projection data is 512 x 360. The projection data on each row are the detector values on the corresponding angle.

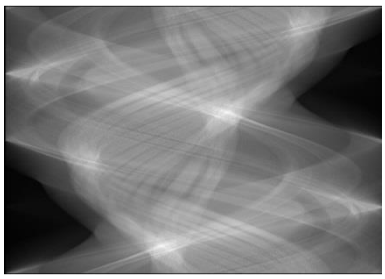

Fig.4.3 The projection data obtained from the artifact-free image in Fig.4.2.

The projection data from images Fig.4.1 and Fig.4.2 were compared. Differences between them were adjusted, so the image with heavy streak artifacts was changed accordingly. The ML-EM reconstruction algorithm was applied. The ML-EM is an iterative restoration method that results in an approximation between the processed image and the target image. The slice with heavy streak artifacts was processed using the adjacent intact slice, i.e., a CT image without major artifacts. The adjacent slices depicted very similar anatomical structures. 50 iterations were carried out for streak artifact reduction. The resultant images are shown in Fig.4.4. Fig.4.4 presented the reconstructed images of 1st (a), 2nd (b), 5th (c), 10th (d), 20th (e), 30th (f), 40th (g), and 50th iteration (h), respectively.

At the initial stage, the image for the 1st iteration is simply the output-field definition (Fig.4.4a). The processed MDCT image at the 2nd iteration is shown in Fig.4.4b. The image is blurred, but the blurring is gradually reduced with further iterations. Heavy streak artifacts from at least four dental metallic prosthetic appliances can be observed on the original image (Fig.4.1). Some of these were clearly removed by the repeated cycles of correction, as shown in Fig.4.4c-g. Finally, only two small streak artifacts in the left molar region were observed after 50 cycles of iterative correction (Fig.4.4h). Anatomical structures were depicted clearly and accompanied by only marginal deviations from the original image after the iterative correction method was executed. More than 20 cycles of the iteration were needed to reduce the metal-induced streak artifacts. We tried more than 50 cycles of the iteration, but the remaining small artifacts were never removed and the noise that existed on the image uniformly increased.

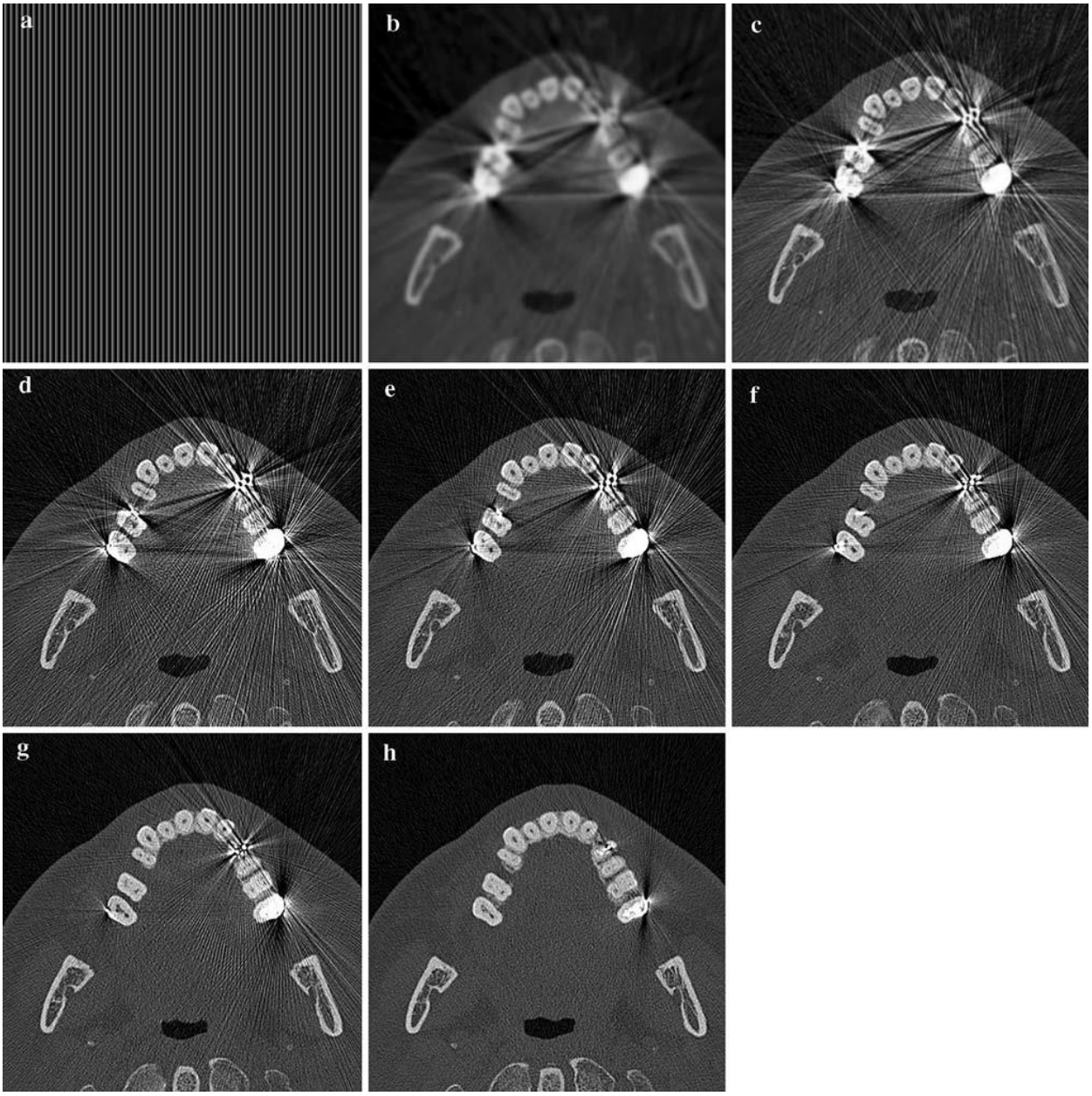

Fig.4.4 Processed MDCT images at **a** the 1st iteration, **b** the 2nd iteration, **c** 5th iteration, **d** 10th iteration, **e** 20th iteration, **f** 30th iteration, **g** 40th iteration, and **h** 50th iteration.

The time required for the iteration calculation of 50 cycles was about 6 min 10 sec. To observe the streak artifact reduction effect, two subtracted images were produced, and they are shown in Fig.4.5a, b. Fig.4.5a shows the subtraction between the initial image having artifacts (Fig.4.1) and the processed image at the 50th iteration (Fig.4.4h). The other is the subtraction between the artifact-free image (Fig.4.2) and the processed image at the 50th iteration (Fig.4h).

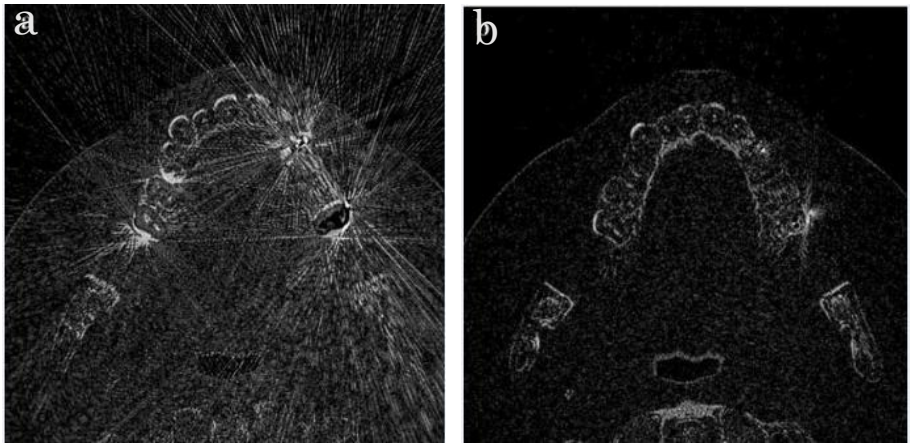

Fig.4.5 Subtracted images between **a** the original image having heavy artifacts in Fig.4.1 and the processed image at the 50th iteration in Fig.4.4h and **b** the artifact-free image in Fig.4.2 and the processed image at the 50th iteration in Fig.4.4h.

4.2 ML-EM method applied to streak artifact reduction in sequential images

In Fig.4.6, twelve continuous images are aligned from head to foot, from no.1, the far left side on the top row, to no.12, the far right side on the bottom row. They are original maxillary images on which streak artifacts appeared. The metal-induced artifacts become heavier as the slice sequence number increases. The thickness of the slices is 0.5 mm, and the image acquisition conditions are the same with that of slices in section 4.1.

In Fig.4.6, thin thickness CT images depict very similar anatomical structures and there are artifact-free slices next to slices having heavy streak artifacts, we attempted to remove or reduce the metal-induced artifacts on 12 sequential images (images in Fig.4.6) using projection data of an artifact-free image. Fig.4.7A shows the artifact-free image which is next to image no.1 of Fig.4.6, and Fig.4.7B shows the artifact-free image's projection data. We used the projection data (Fig.4.7B) to do streak artifact reduction to each image in Fig.4.6 by ML-EM algorithm.

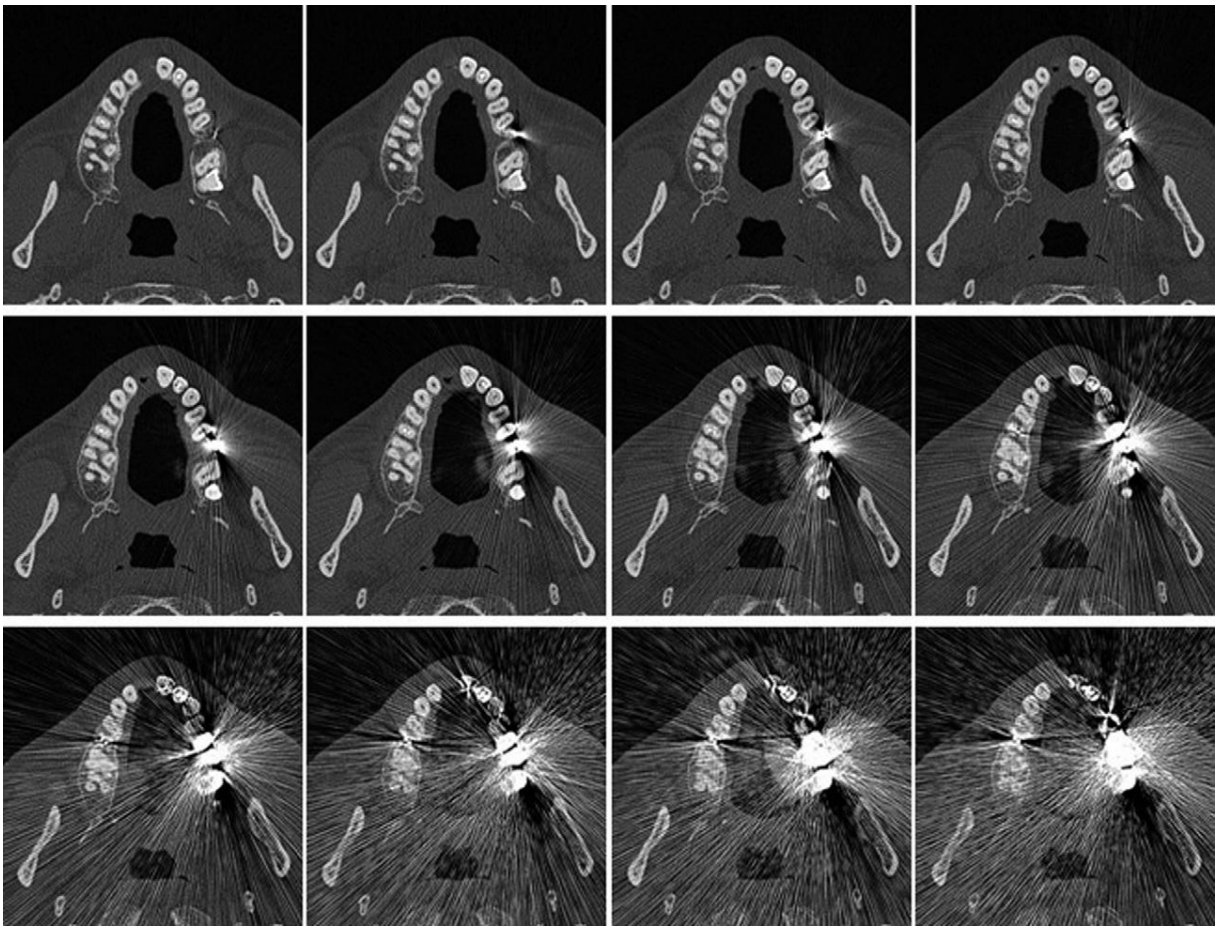

Fig.4.6 twelve continuous images are aligned from head to foot, from no.1, the far left side on the top row, to no.12, the far right side on the bottom row. They are original maxillary images on which streak artifacts appeared and objects for the proposed processing.

In section 4.1, we proved that the optimum iteration times of ML-EM algorithm is 50 for streak artifact reduction in X-ray MDCT images. Here we also set the iteration times as 50 accordingly.

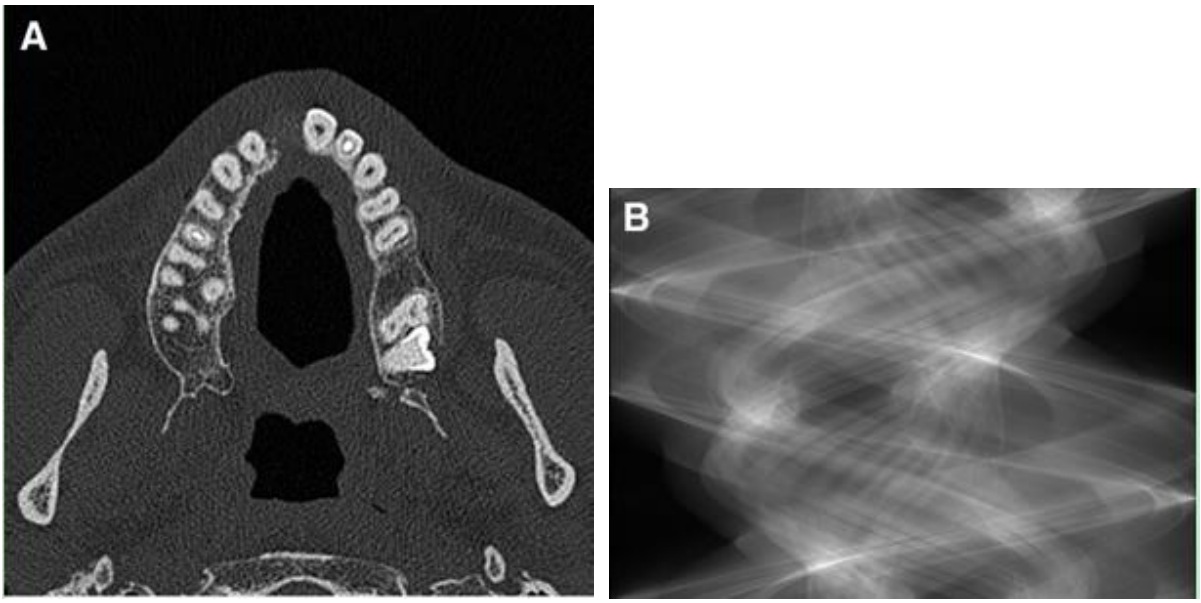

Fig.4.7 **A**, the artifact-free/intact image, which is next to image no.1 of Fig.4.6. **B**, the projection data computed from the artifact-free image of Fig.4.7A.

The continuous 12 images in Fig.4.8 were reconstructed by the ML-EM algorithm using the same projection data of the intact image. These maxillary images correspond to the 12 images in Fig.4.6. Streak artifacts were reduced sequentially. Weak streak artifacts were reduced effectively on the forward images, especially the lightening parts were depressed availably. Radiate lines on the background were also removed. However, some artifacts still remained on the latter images which contained heavy streak artifacts. What's more, some deviations occurred on anatomical structures on both teeth and soft tissues. The reason is considered to be the differences between the artifact-free image and the processed images.

ML-EM algorithm realized the metal-induced streak artifact reduction on sequential MDCT images. Iteration times was set to 50 according to the conclusion in section 4.1.

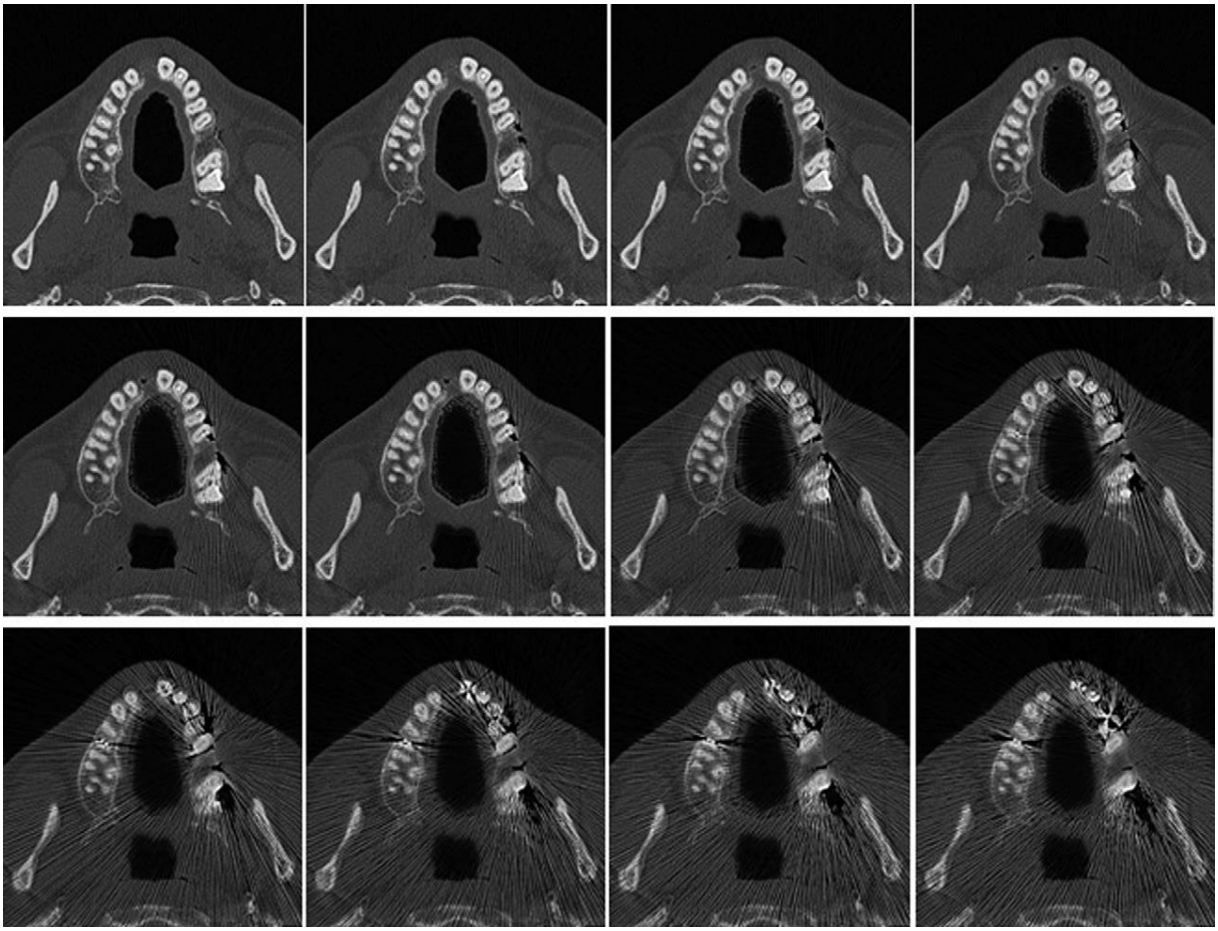

Fig.4.8 The reconstructed 12 images by ML-EM algorithm using the same artifact-free image's projection data. They correspond to the order of Fig.4.6.

4.3 OS-EM variable optimization in streak artifact reduction

OS-EM algorithm is considered to be the solution for fast image reconstruction [21, 22]. The image quality factor, namely the image update number, is the product of subset numbers and iteration times.

$$\text{Image update number} = \text{subset number} \times \text{iteration times}$$

Image quality of reconstructed images differs according to the parameter setting of OS-EM algorithm. In this section, we designed four parameter combinations for OS-EM algorithm to examine effect in streak artifact reduction. Four parameter combinations are shown in Table.4.1 as group A, B, C and D.

Table.4.1 Parameter combination of OS-EM

	A	B	C	D
Subset number	8	8	4	4
Iteration time	5	10	10	5

The artifact-free image and its projection data is shown in Fig.4.9. The initial image with heavy metal-induced streak artifact is shown in Fig.4.10. The OS-EM algorithm program was carried out respectively according to the parameter combinations. In the first execution, we set the subset number = 8 and iteration time = 5. The result image is shown in Fig.4.11a. In the second execution, we set the subset number =8 and iteration time = 10. The result image is shown in Fig.4.11b. As so on, the result of c and d are shown in Fig.4.11c and Fig.4.11d.

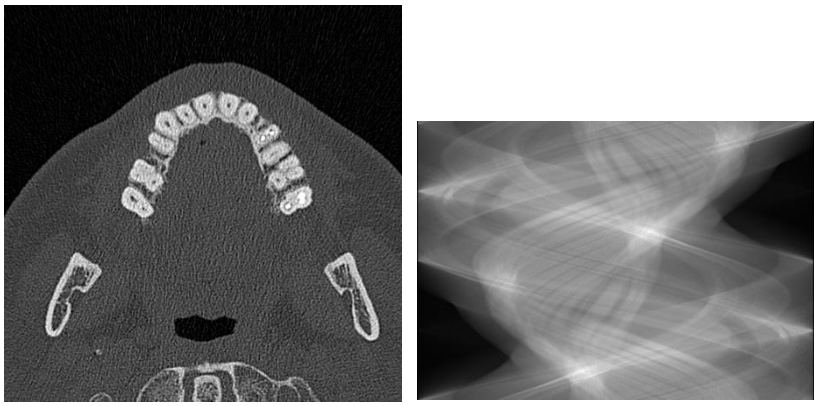

Fig.4.9 The artifact-free image (on the left) and its projection data (on the right).

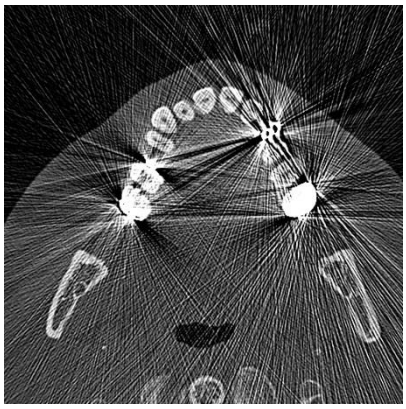

Fig.4.10 MDCT image with heavy streak artifacts. The processing object.

Metal-induced streak artifacts were reduced in the result images (Fig.4.11). Radiate artifact lines on the background were removed on each image. However, streak artifacts on the maxillary sinus and maxilla still remained. Comparing the four result images, streak artifacts on image b were reduced at the greatest degree. The streak artifact distribution is minimum on maxilla compared to other 3 images, especially in the area circled in red. Images a and c presented very similar artifact reduction effect. Streak artifacts on image d were remained the most. Besides, deviations on teeth edge appeared on each result image. The reason is thought to be that the anatomical structures on target image and proceeded image differed to a large degree.

The artifact reduction effect of the four result images is just in proportion to the image update number. The more times image was updated, the better artifact reduction effect was obtained. On the other hand, if the image update number is too large, the image will be depicted to almost the same with target image, which causes more deviations appear on result image. Thus, the parameter combination, subset = 8 and iteration = 10 was selected as the optimal combination for OS-EM algorithm [25].

Table. 4.2 shows the processing time of OS-EM algorithm under different parameter settings. It could be concluded that the processing time is in proportion to iteration times. More iterations causes more processing duration. Compared to the processing time of ML-EM algorithm, OS-EM algorithm is a time-saving method. It requires more than 6 min to reconstruct a 512 x 512 CT slice using ML-EM algorithm (50 iterations). While the processing duration is reduced to about 80 sec by OS-EM algorithm with 10 iterations, and it is about 44 sec if the iteration times is 5.

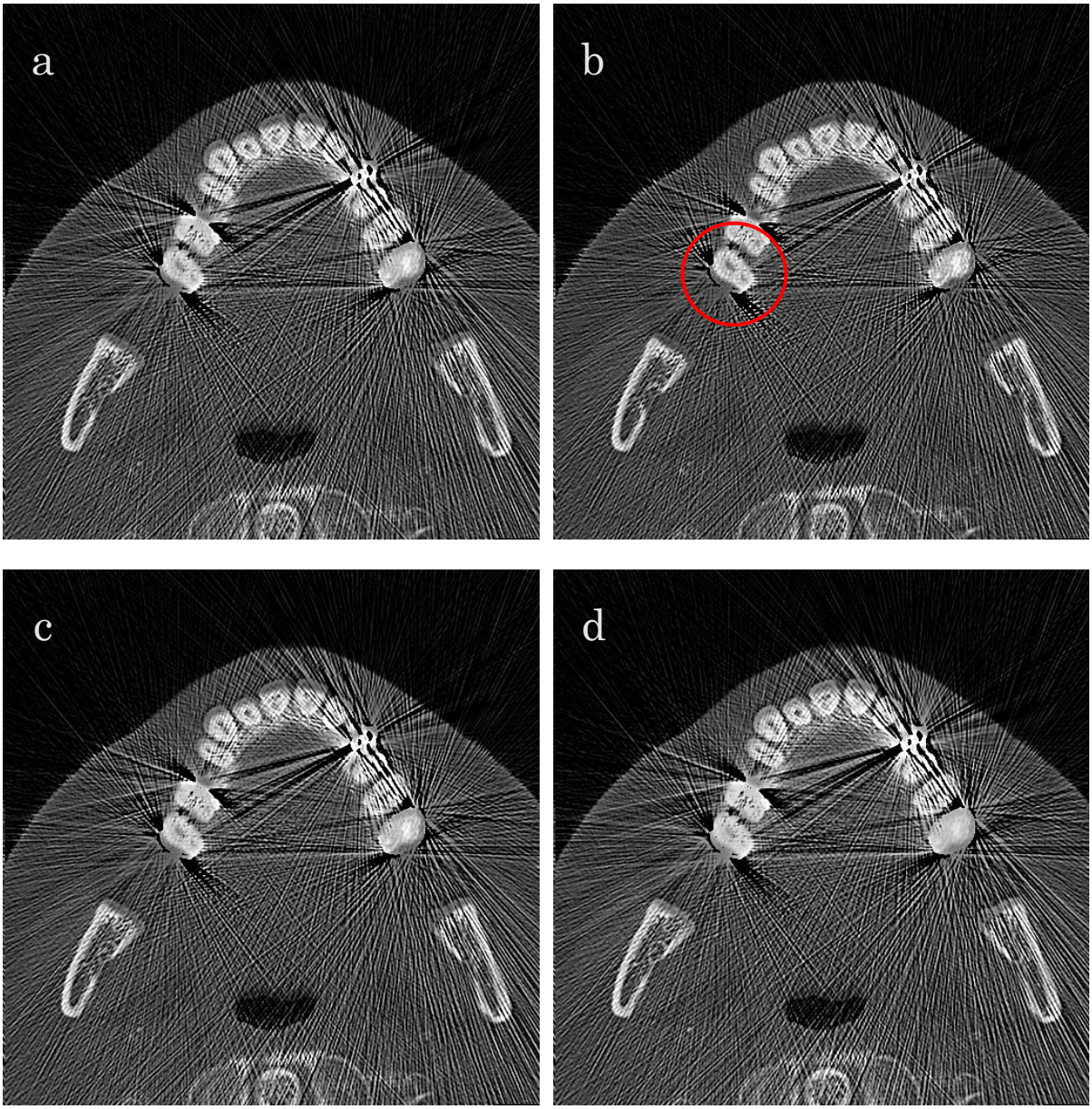

Fig.4.11 Result images processed by OS-EM algorithm with different parameter settings. **a**, subset = 8, iteration =5. **b**, subset = 8, iteration = 10. **c**, subset = 4, iteration = 10. **d**, subset = 4, iteration = 5.

Table.4.2 Processing time of OS-EM under different parameter setting

	A	B	C	D
Subset number	8	8	4	4
Iteration time	5	10	10	5
Processing time	44.15 s	84.25 s	82.47 s	42.20 s

Chapter V. Successive iterative restoration applied to streak artifact reduction in X-ray CT image of dento-alveolar region

5.1 Successive iterative reconstruction method (SIRM)

Since comptued tomography's intruduction in the 1970s, CT has become an improtant tool in medical imaging to supplement X-ray radiographic examinations[1, 4]. It has more recently been used for preventive medicine or screening for disease. For example CT colonography for patients with a high risk of colon cancer, or full-motion heart scans for patients with high risk of heart disease. Besides, CT has increasingly been used by dentists and oral specialists who want three-dimensional images to assist with complicated procedures. Dentists who have CT scanners say the machines deliver a superior three-dimensional image that can be examined from every angle. That allows them to see details like the location of nerves and sinuses before inserting implants or performing oral surgery, which can avoid serious complications.

CT modality produces tomographic images of specific areas of the scanned object, allowing the user to see what is inside it without cutting it open. To reduce the partial volume effect, thin thickness CT slices are commonly produced. Especially in the dental used CT modality, CBCT, has a range of slice thicknesses available. It is usually between sub-0.1 mm to 0.4 mm slice thickness. The adjacent thin thickness CT slices are depicting very similar anatomical structures. In the dento-maxillofacial region slices, streak artifacts can be observed when the metallic prosthetic appliances with high atomic numbers are used, and in many cases, artifact-free image exists in neighbor. Thus, we proposed the successive iterative reconstruction method (SIRM) to process the sequential CT images for streak artifact reduction [21, 22]. First the projection data of the artifact-free slice was obtained. The adjacent slice, which showed weak artifacts, was processed using

the artifact-free slice's projection data. Then the projection data of the newly processed image was obtained and was used to reconstruct the next image which contained a little more artifacts. In this manner, the processing by the iterative restorations (ML-EM algorithm and OS-EM algorithm) and the computation of the projection data were repeated [21-23]. The process of the successive iterative reconstruction method is descripted in Fig. 5.1.

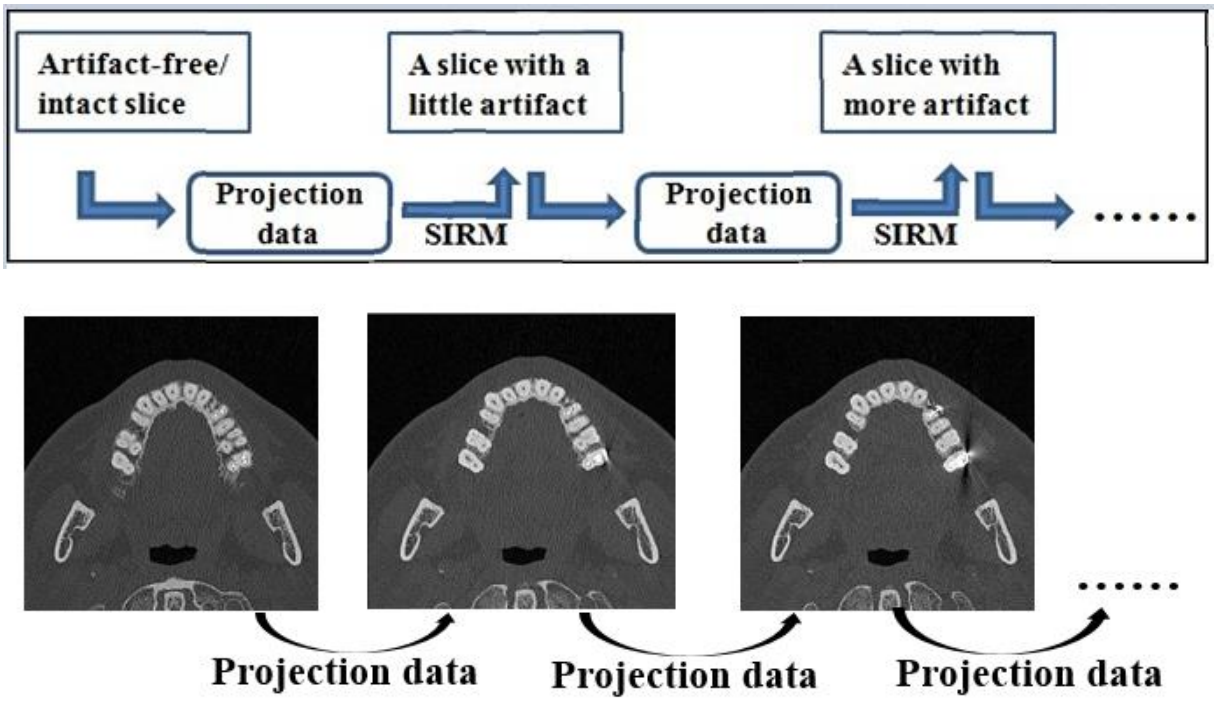

Fig.5.1 The process of successive iterative reconstruction.

5.2 Streak artifact reduction by successive iterative ML-EM

We applied the maximum likelihood-expectation maximization (ML-EM) reconstruction algorithm to multi detector computed tomography (MDCT) images. We used the same MDCT slice series of the maxillary sinus and maxilla with that in section 4.1. The slice acquisition was carried out using a Somatom® Plus 4 Volume Zoom (Siemens, Erlangen, Germany). Principal exposure parameters were as follows: 120 kV, 130 effective mAs, and a slice thickness of 0.5 mm. The pixel matrix of each slice was 512 x 512. Severe metal-induced streak artifacts occurred

at several tooth crowns in the maxilla, and in addition, the overlapped regions were invisible.

The MDCT images with streak artifacts were selected as shown in Fig.5.2, and they were objects of our proposed successive iterative reconstruction method. The patient consented to the use of CT images for the study. Continuous twelve images in order from head to foot are shown. We focused on the processing on CT images of maxillary teeth and surrounding region. The adjacent image to Image No.1 (the far left image on the top row in Fig.5.2) is a streak artifact-free/intact slice, and it is shown in Fig.5.3 a.

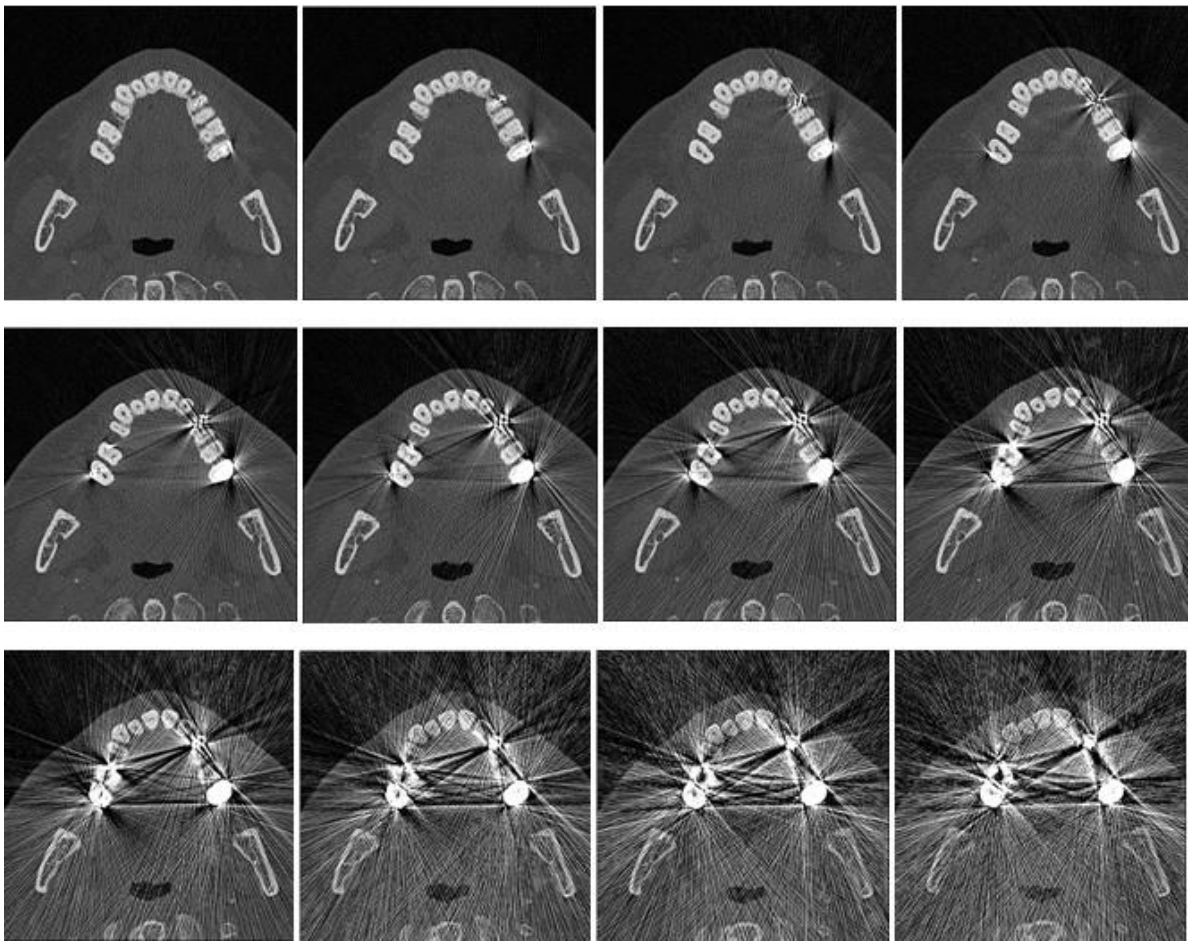

Fig.5.2 Continuous twelve images are aligned from head to foot, from No.1, the far left side on the top row, to No.12, the far right side on the bottom row. These are original images on which streak artifacts appeared and objects for the proposed processing.

Projection data acquisition was carried out as described in section 3.1. The projection data were acquired at 360 directions with 1 degree intervals. Projection data acquisition of an image next Image No.1 in Fig.5.2 was carried out at first. Our trial was to reduce streak artifacts from Image 1 in Fig.5.2 using the projection data of the intact image in neighbor. And successively, Image No.2 in Fig.5.2 was processed using the projection data of the processed Image No.1 and went to the next succeeding ones. The artifact-free image and its projection data are shown in Fig.5.3a, b. Also, the projection data of Image No.5 in Fig.5.2, as an example, are shown in Fig.5.3c. The projection data in Fig.5.3b, c are usually called the sonogram. Comparing the projection data of two images, the sonogram corruption by the metal presence is observed in Fig.5.3c, and some chain like noise can be observed in the projection data (Fig.5.3c).

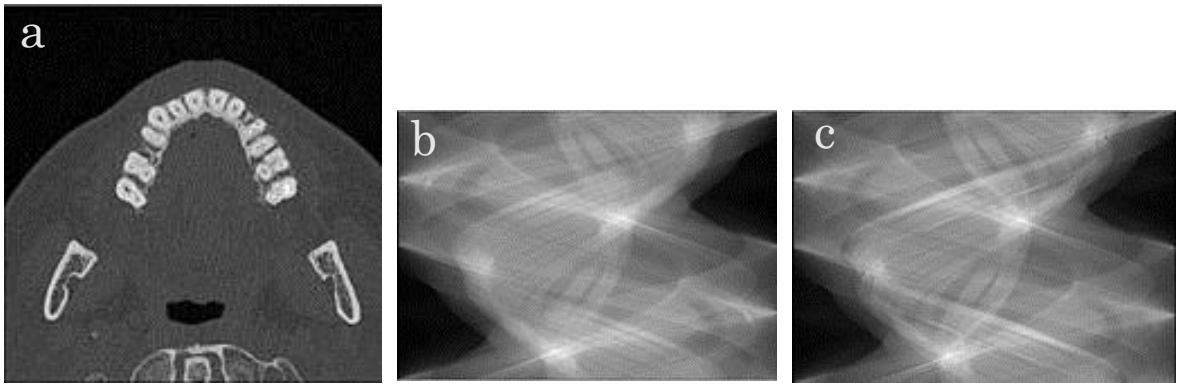

Fig.5.3 **a** the image obtained from the artifact-free/ intact image, which is next to Image No.1 in Fig.5.2. **b** the projection data obtained from a. **c** the projection data of Image No.5 in Fig.5.2.

Fig.5.4 shows twelve reconstructed images by the proposed successive iterative reconstruction method. There images are corresponding to twelve images in Fig.5.2. The ML-EM algorithm was carried out 50 iterations to images using the projection data of the immediate neighboring processed image. Namely, Image No.2 was processed using the processed Image No.1' projection data, and the Image No.3 was

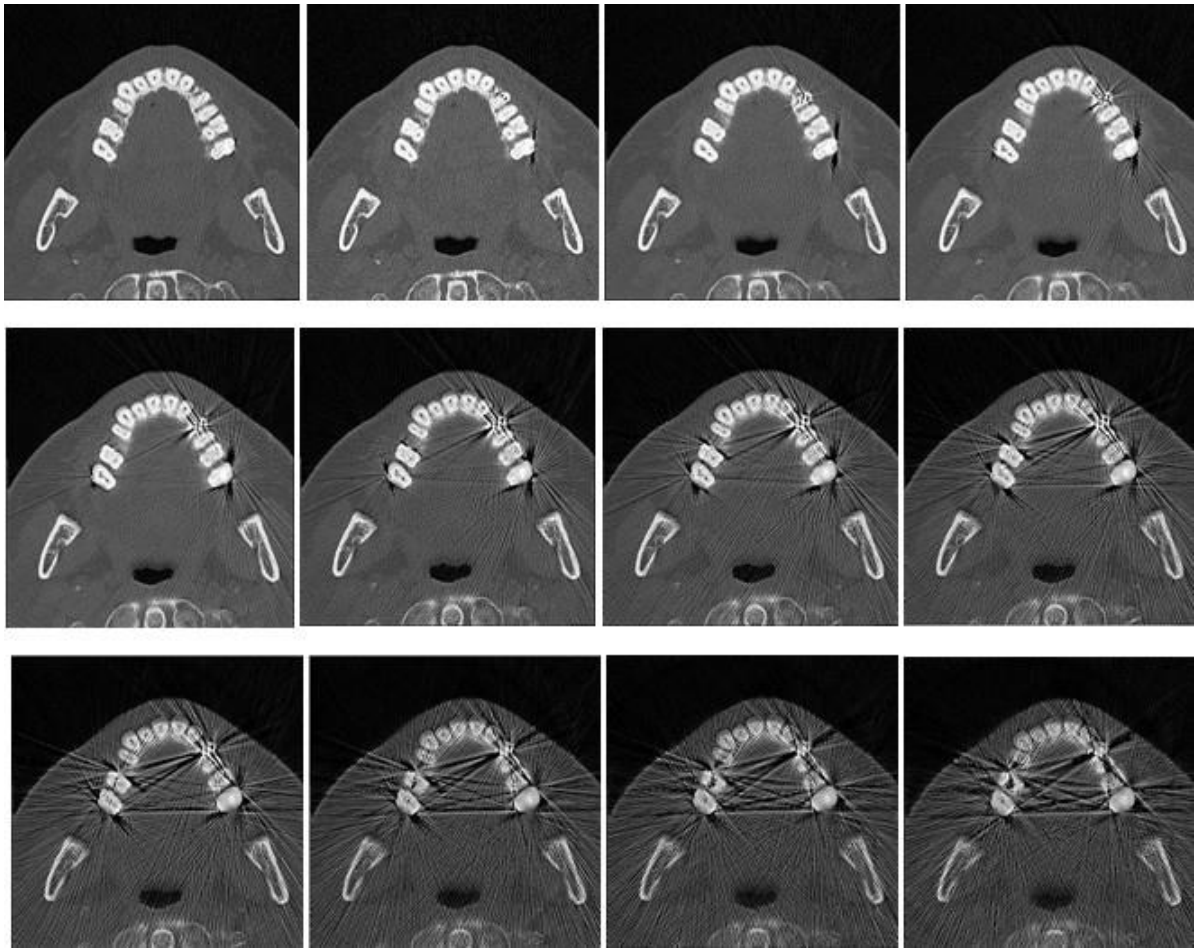

Fig.5.4 Processed images of Image No.1 to No.12, corresponding to twelve images in Fig.5.2.

processed using the processed Image No.2, and the processing was carried out to Image No.12 in the same way. After the processing, streak artifacts were reduced obviously, but some of them never disappeared on the images containing heave streak artifacts.

Twelve subtracted images are shown in Fig.5.5. They are subtracted images between the original images (Images No.1 to No.12 in Fig.5.2) and processed images (Image No.1 to No.12 in Fig.5.4), respectively. Subtracted images presented the amount of reduced streak artifacts by the processing. Besides, subtracted images also showed the deviations occurred on the edge of teeth and some soft tissues.

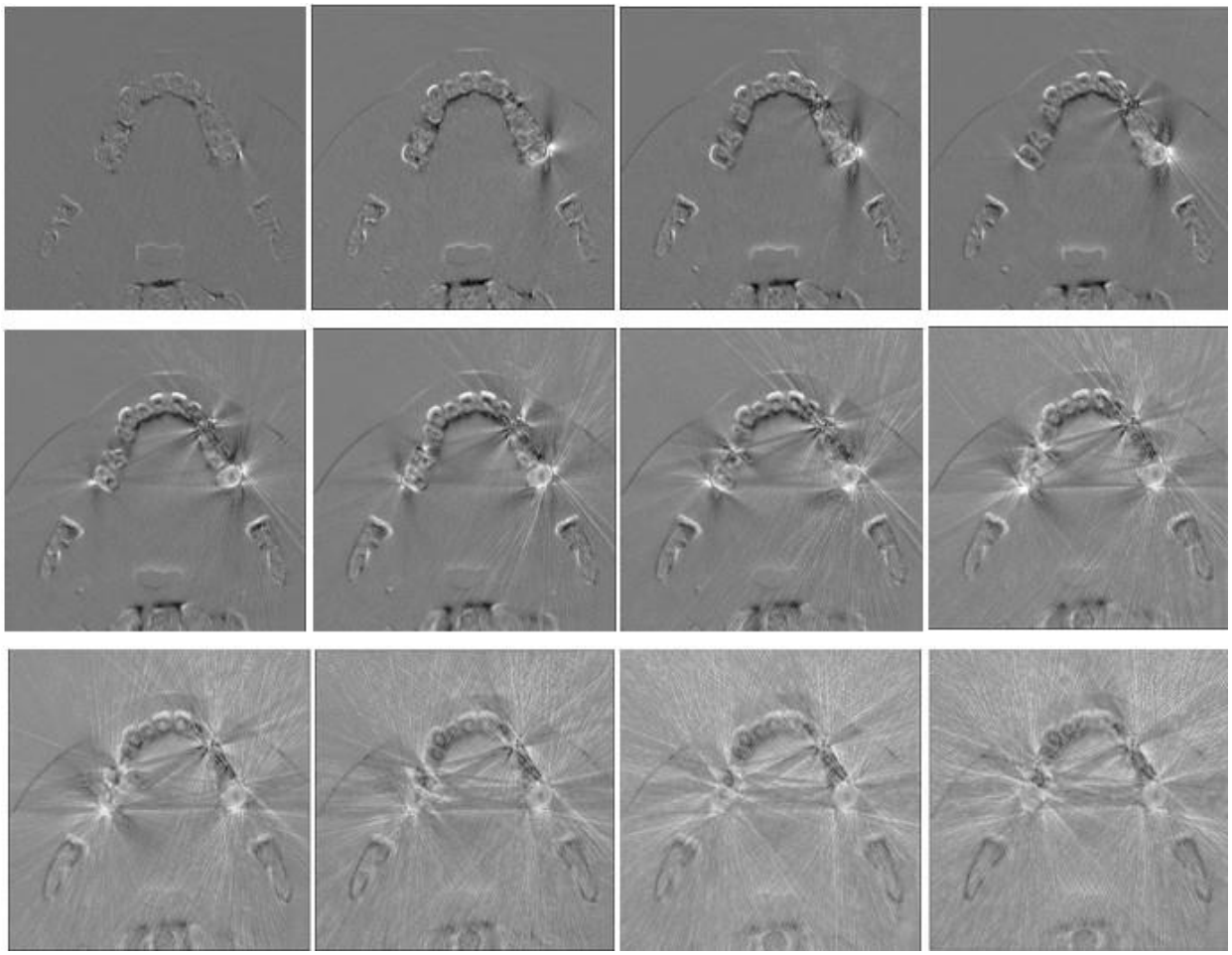

Fig.5.5 Twelve subtracted images between twelve original images in Fig.5.2 and their processed images in Fig.5.4.

To prove the general purpose properties of successive iterative ML-EM algorithm for streak artifact reduction, we applied it to another dento-maxillofacial image case. The original images are shown in Fig.5.6, which are the same images with Fig.4.6. Similarly in this case, streak artifacts are also observed seriously, and some overlapped areas lost the diagnostic value. The artifact-free image which is next to Image No.1 of Fig.5.6 is shown in Fig.5.7a, and the projection data of Fig.5.7a is shown in Fig.5.7b. Fig.5.8 shows 12 resultant images processed by the successive iterative ML-EM algorithm. These maxillary images correspond to the 12 images in Fig.5.6.

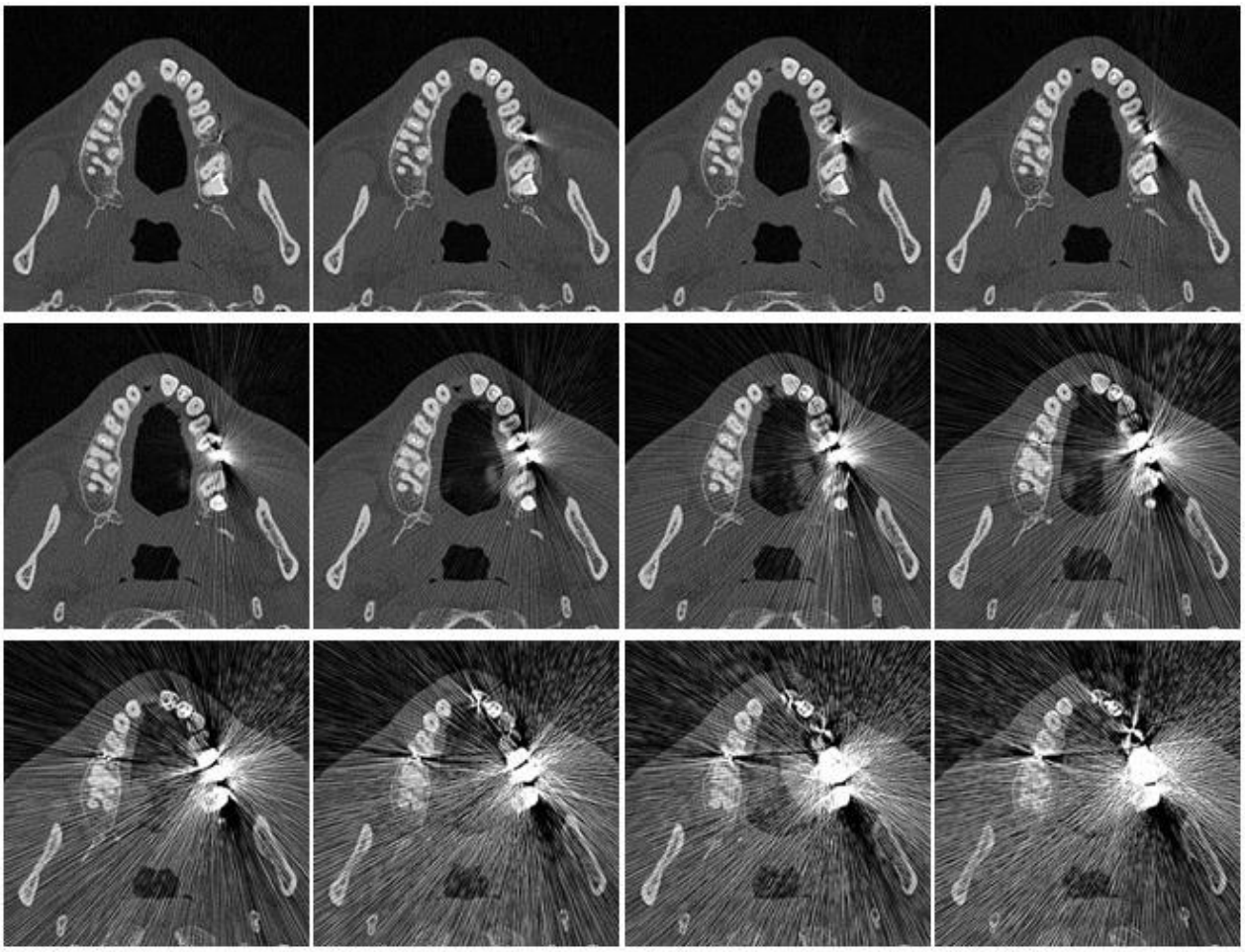

Fig.5.6 Twelve continuous images are aligned from head to foot. They are original maxillary images on which streak artifacts appeared and objects for the proposed processing.

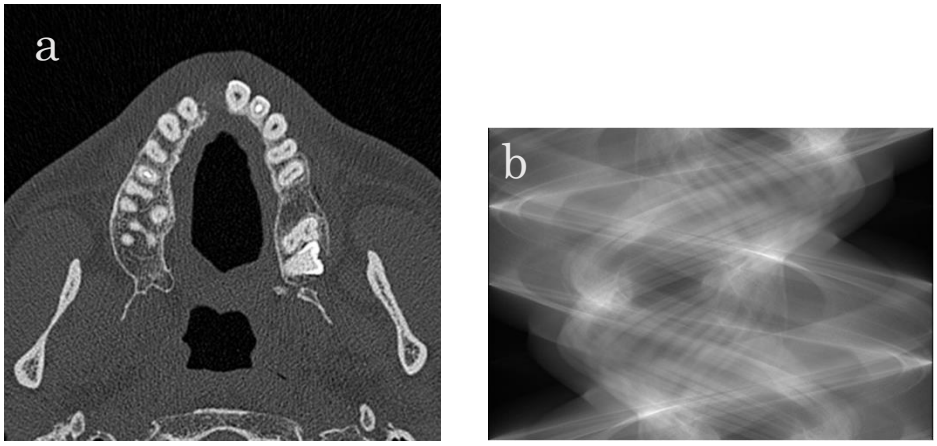

Fig.5.7 **a**, the artifact-free image, which is next to Image No.1 in Fig.5.6. **b**, the projection data of Fig.5.7a.

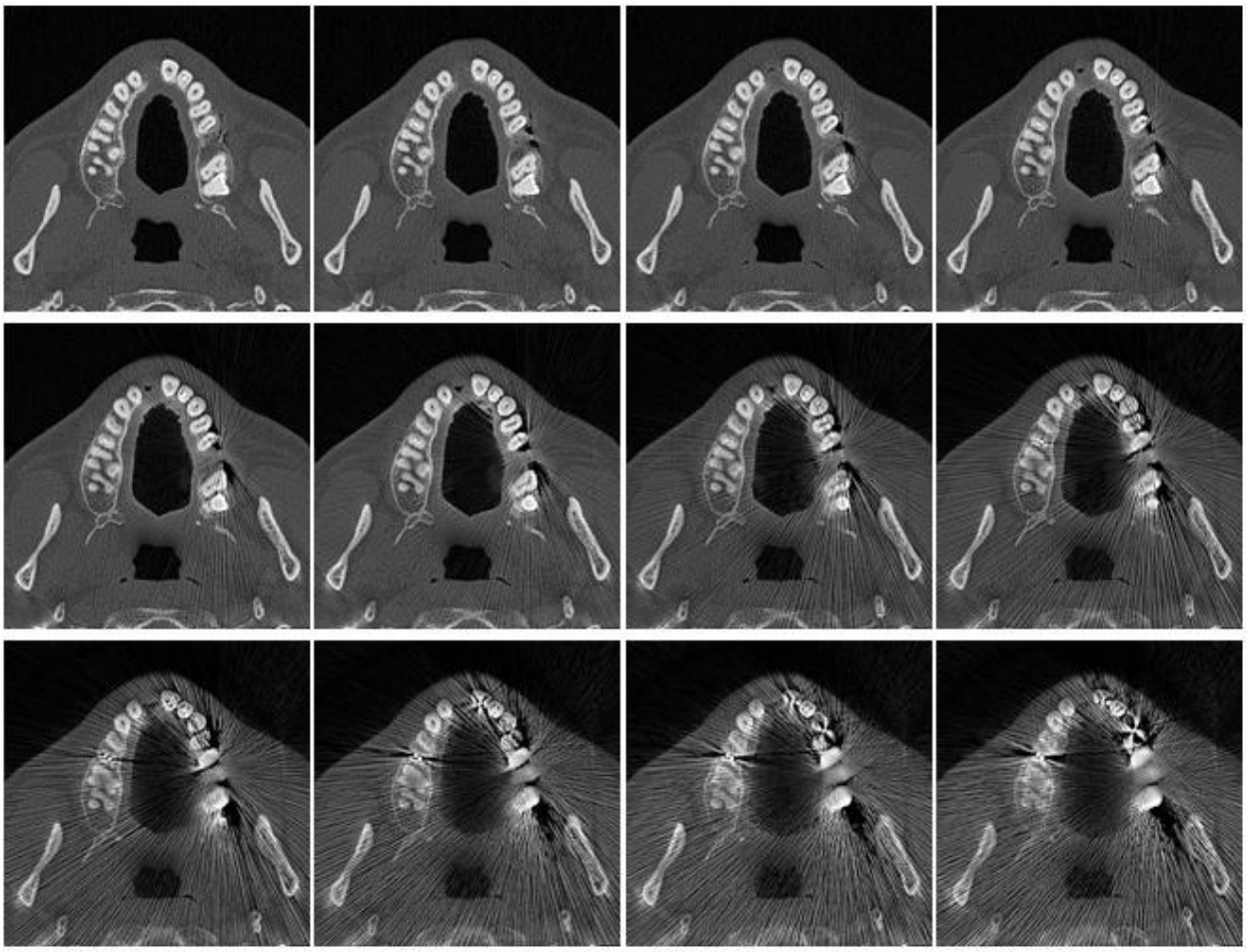

Fig.5.8 Reconstructed images by successive iterative ML-EM algorithm. They correspond to the 12 images in Fig.5.6.

We applied the novel method, namely to use the adjacent CT images that often depict very similar anatomical structures, to CT images having very heavy streak artifacts. Appearances of streak artifacts are case by case, the comparison of effectiveness with prior methods is sometimes difficult, but the heavy artifacts reduction was achieved by successive iterative ML-EM restoration. The weak streak artifacts were removed.

The cycle of iterations was set as 50 in this section, due to the results of section 4.1. Iterations were tried to 100 cycles practically, but no significant changes in artifact appearances were shown.

5.3 Streak artifact reduction by successive iterative OS-EM

We applied the successive iterative OS-EM algorithm to sequential images for streak artifacts reduction. We also used the images in Fig.5.6 as the original images. An artifact-free image which is next to the Image No.1 of Fig.5.6 is shown in Fig.5.7a, and the projection data of Fig.5.7a is shown in Fig.5.7b.

Fig.5.9 shows 12 resultant images processed by the OS-EM successive iterative algorithm. These maxillary images correspond to the 12 images in Fig.5.6. The projection data used were generative ones. Namely, image No.2 was processed using the projection data of reconstructed image No.1, and image No.3 was processed using reconstructed image No.2 and so on. In this processing, we set subset number as 8, and iteration time as 10. Thus, each image was updated 80 times. Artifacts seemed to be reduced similar to those in Fig.5.8. The second molar tooth on the left mandible was overlapped absolutely with artifacts in the original image; however, after the processing it became clear to some extent.

The streak artifacts in the images were caused by implant denture. Today, with the improvement of orthodontics, orthodontic wire and brackets, bone screws or titanium plates are very common especially on teenagers. The streak artifacts caused by the appliances are also unavoidable in CT scans. The successive iterative restoration method should be examined in streak artifact reduction where the artifacts are induced by orthodontic appliances.

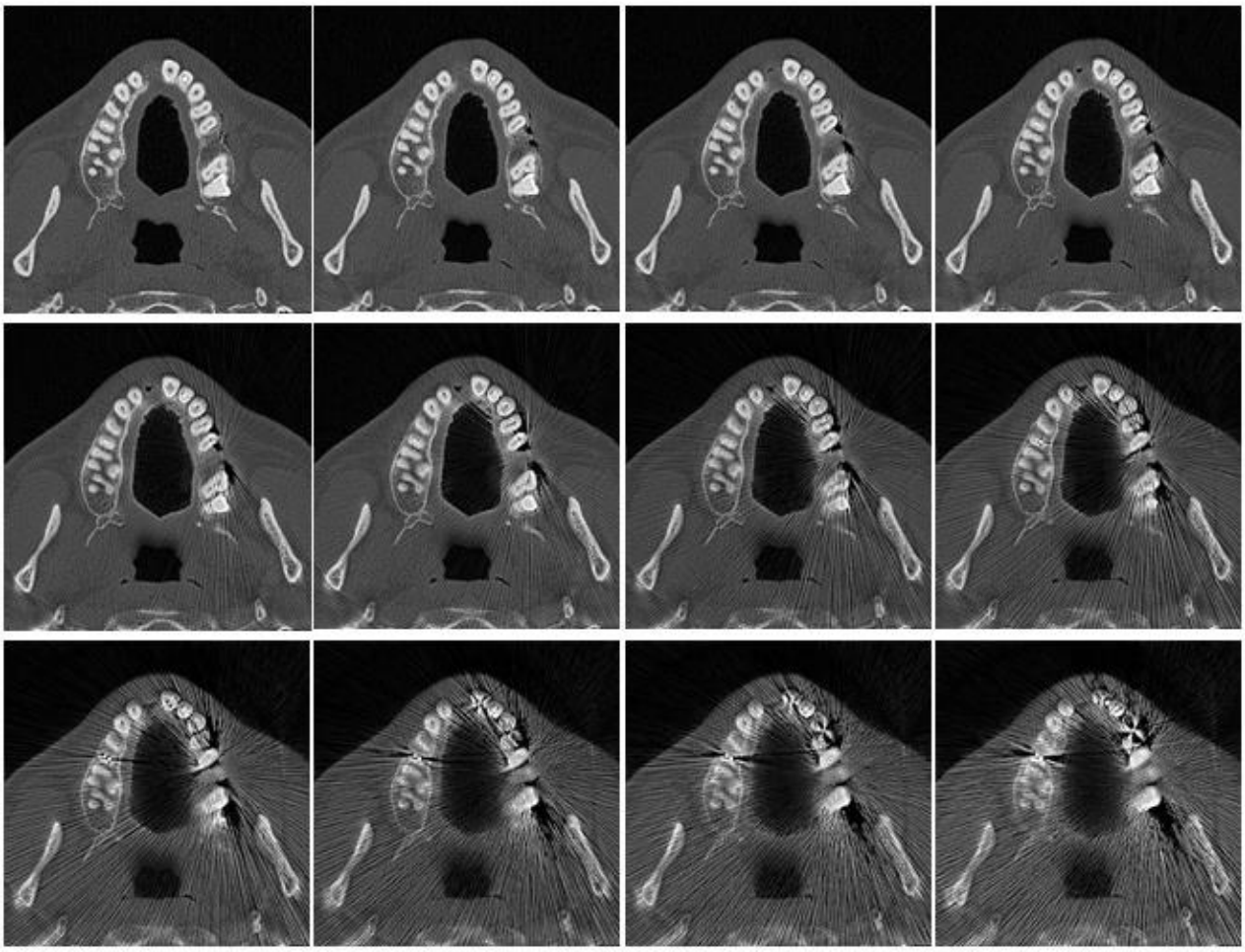

Fig.5.9 Reconstructed images of Image No.1 to No.12 by successive iterative OS-EM algorithm. They correspond to the 12 images in Fig.5.6.

We have processed the same case images by 3 methods until this section. The methods we used were single ML-EM algorithm, the successive iterative ML-EM algorithm and the successive iterative OS-EM algorithm. Their results are shown in Fig.4.8, Fig.5.8 and Fig.5.9 respectively. To show an intuitive comparison of the results from different methods, we created zoomed pictures based on respective resultant images. The zoomed pictures are shown in Fig.5.10. The 2 images in the first column were taken from original images in Fig.5.6. They are zoomed pictures from molar and mandibular ramus regions in No.4 and No.8 images of Fig.5.6. And as so on, the 2 images in the second column were taken from Fig.4.8. They are zoomed pictures from molar and mandibular ramus regions in No.4 and No.8 of

Fig.4.8. The images in the third and fourth column were taken from the same parts of Fig.5.8 and Fig.5.9. By observing the zooming pictures, it can be concluded that streak artifact reduction was achieved by each processing method, but large differences between the results were not obvious.

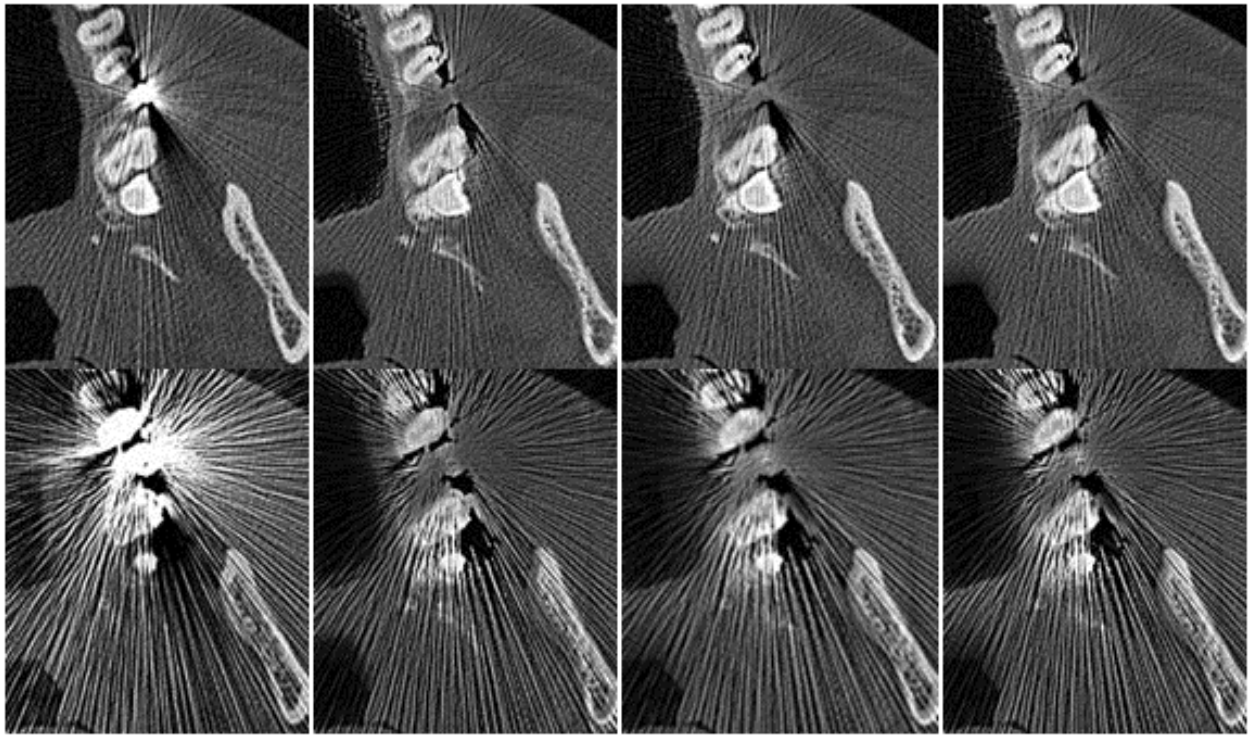

Fig.5.10 Zooming pictures. The 2 images in the first column were taken from original images. They are zooming pictures from molar and mandibular ramus regions in No.4 and No.8 images of Fig.5.6. And so on, the 2 images in the second column were taken form Fig.4.8. They are zooming pictures from molar and mandibular ramus regions in No.4 and No.8 images of Fig.4.8. The images in the third and fourth column were taken from the same parts of Fig.5.8 and Fig.5.9 respectively.

5.4 Region of interest setting

Because streak artifacts appeared only surrounding the teeth, we did the segmentation to CT slices to restrict only the teeth region. A simple rectangular region of interest (ROI) was used for the segmentation [21]. The same original images in Fig.5.6 were used for segmentation. Pixel matrix of each segmented slice was 512 x 295. The segmented artifact-free slice and its projection data are shown in Fig.5.11, a and b. The projection data were calculated only from the teeth area;

therefore, the density of the center part became brighter in the projection data image, and comparatively the soft tissue components seemingly disappeared at the image peripherals. The pixel matrix of the projection data was 512 x 360.

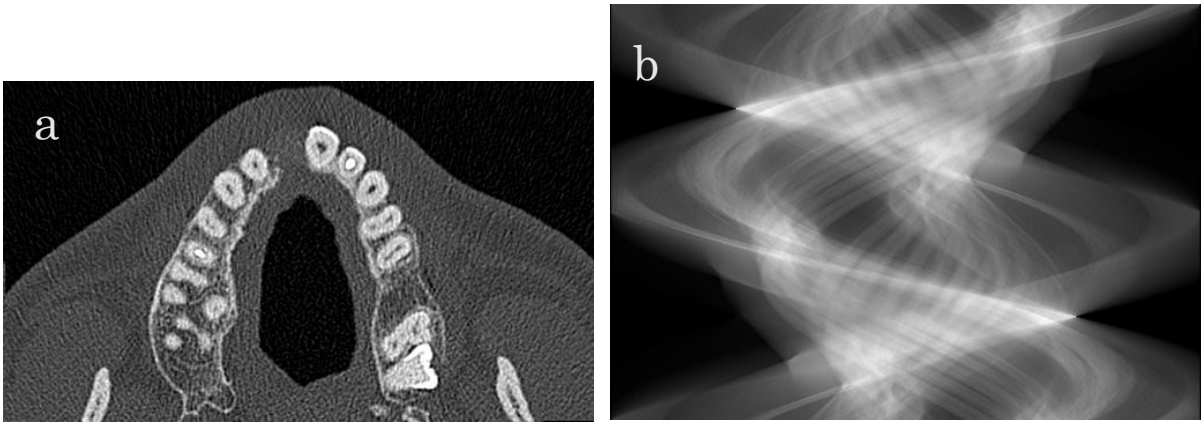

Fig.5.11 **a**, the segmented artifact-free/intact image, whose original image is next to image No.1 of Fig.5.6. **b**, the projection data computed from Fig.5.11a.

The segmented ROI images were also processed by the OS-EM successive iterative algorithm in the condition of the optimal parameter combination, and the results are shown in Fig.5.12. The teeth region was reconstructed without the influence of posterior tissues, and streak artifacts were reduced. The processing time were also reduced largely.

There are two advantages of ROI image segmentation. On one hand, during image reconstruction, influence from posterior tissue structure was removed. On the other hand, the processing time for reconstructing one image was shortened significantly, to about a half. The segmentation was done by cutting the top and bottom parts without teeth structure, and we are considering segmenting the image along the maxillary edge line in the next step.

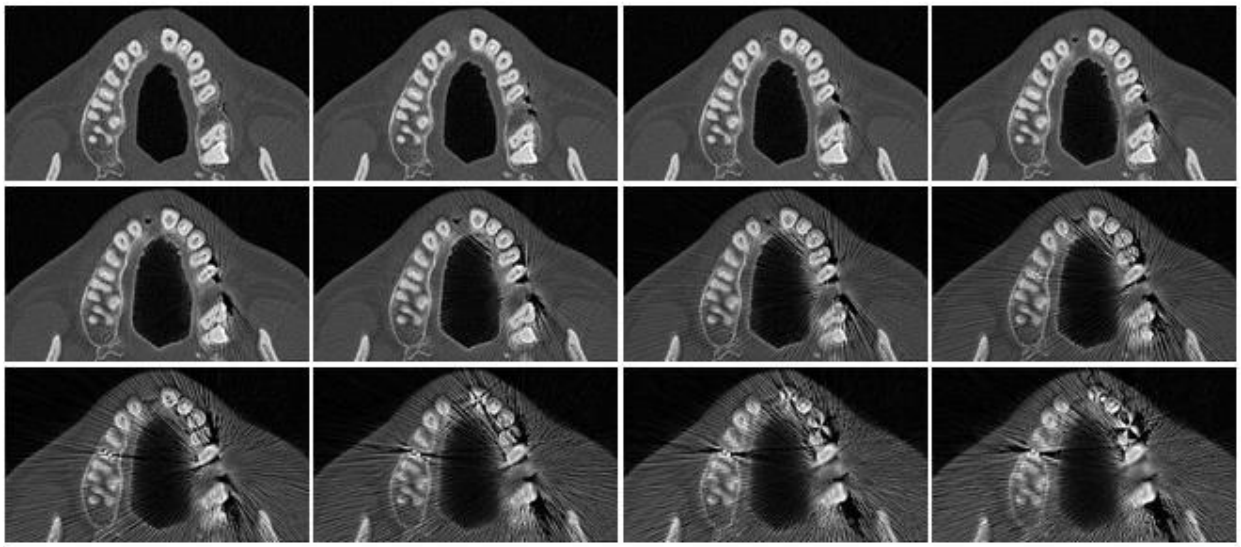

Fig.5.12 Reconstructed ROI images of image No.1 to No.12 by successive iterative OS-EM algorithm. They correspond to the 12 images in Fig.5.6.

Table 5.1. The duration time ratio of each method

ML-EM	*Successive ML-EM*	*Successive OS-EM*	*Successive OS-EM with ROI*
1.0	1.0	0.227	0.124

ML-EM, maximum likelihood-expectation maximization algorithm;
OS-EM, ordered subset-expectation maximization algorithm;
ROI, region of interest.

Processing time is an important factor for clinical operation. Table 5.1 shows the duration time ration of each method. It took 6 minutes 10 seconds for processing a slice by the ML-EM algorithm and we regarded the time as 1 unit. It demonstrated that the OS-EM algorithm is a time saving method. The ROI segmentation processing can further shorten the processing time to about one-eighth of the ML-EM method. The time required for the calculation was not only dependent on the PC performance, but also dependent on the amount of streak artifacts. Streak artifacts usually have a high density value and just it caused the complexity of computation.

5.5 Reverse processing

As described in the previous sections, the successive processing was carried out mainly on the maxillary region, and CT slices were processed along the head-to-foot direction. We call this forward processing. On the other hand, we tried the reverse processing in the mandible region, as shown in Fig.5.13. Namely, the successive processing carried out along the foot-to-head direction [21].

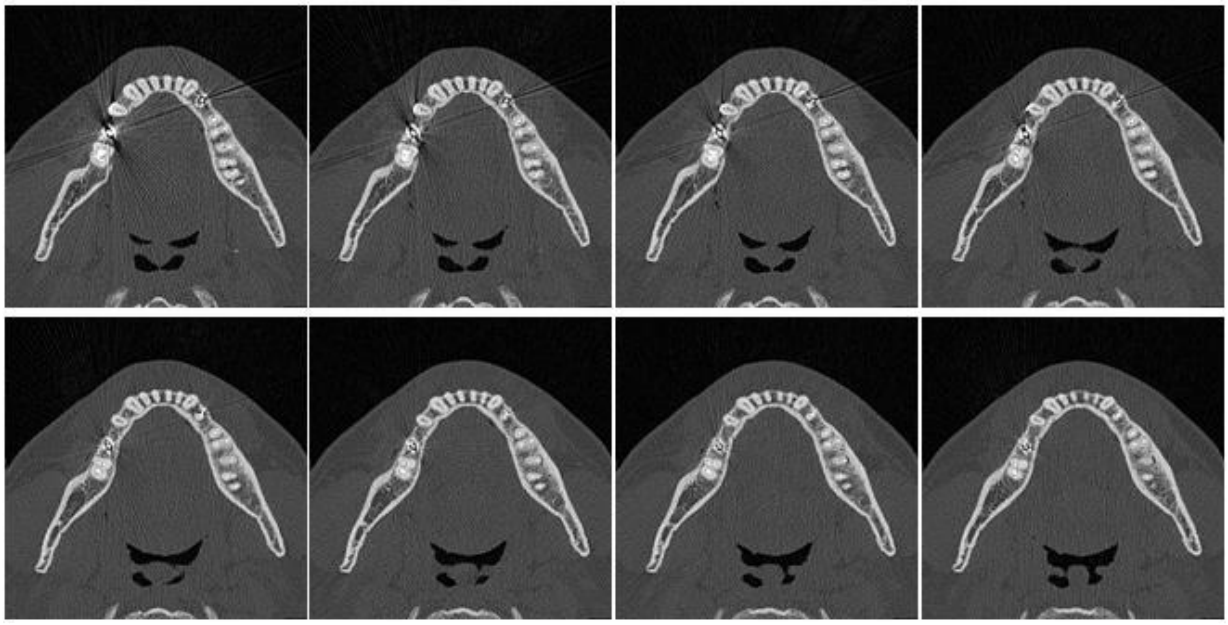

Fig.5.13 Eight continuous lower jaw images aligned from head to foot. The artifact-free image did not exist because of the range of exposures.

We did reverse processing to 7 mandible images, as shown in Fig.5.13. The bottom right image was used for a quasi-intact image. The successive iterative OS-EM algorithm was used and the same above-mentioned optimal combination parameter setting (subset = 8, iteration = 10) was chosen. First, the projection data of image No.8 (at the far-right on the bottom row) in Fig.5.13 was achieved, then applied the projection data to reconstruct neighboring image No.7. The reconstructed image No.7 was used to reconstruct image No.6 and so on.

The reconstructed images are shown in Fig.5.14. Because there existed a little

streak artifacts even on the assumed intact image (No.8) of mandible slices, streak artifacts were not reduced exhaustively.

Fig.5.14 Reconstructed lower jaw images of No.1 to No.7 by successive iterative OS-EM algorithm.

The iterative restoration is an approximation process to the target image. It is important to select a target image. For the maxillary images, streak artifacts appeared gradually, so we can get the artifact-free image, which serves as the target image. The projection data calculated from the artifact-free image was not influenced by artifacts and that is the key point for the successful reduction. On the contrary, in the reverse processing of the mandible images, there was not an image without streak artifacts, so in the resulting images, some of streak artifacts never disappeared.

Chapter VI Application to orthodontic apparatuses and calculation acceleration by GPGPU

6.1 SIRM used in a mandibular retraction case

In this section, MDCT image volumes used for the clinical diagnosis of the jaw deformity were processed [22].

The subject was a 32-year-old female at the time of pre-surgical imaging and had been subsequently re-imaged following surgery. An institutional review board approval was forthcoming. The subject consented to the use of her CT images for this study. The image volumes were acquired using a LightSpeed® VCT (GE Healthcare Japan, Tokyo). The exposure parameters were 120 kV and 361 mAs, and the slice thickness was 1.3 mm. The pixel matrix of each slice was 512 x 512. Severe metal-induced streak artifacts occurred owing to several metallic tooth crowns in the maxilla and mandible and orthodontic appliances.

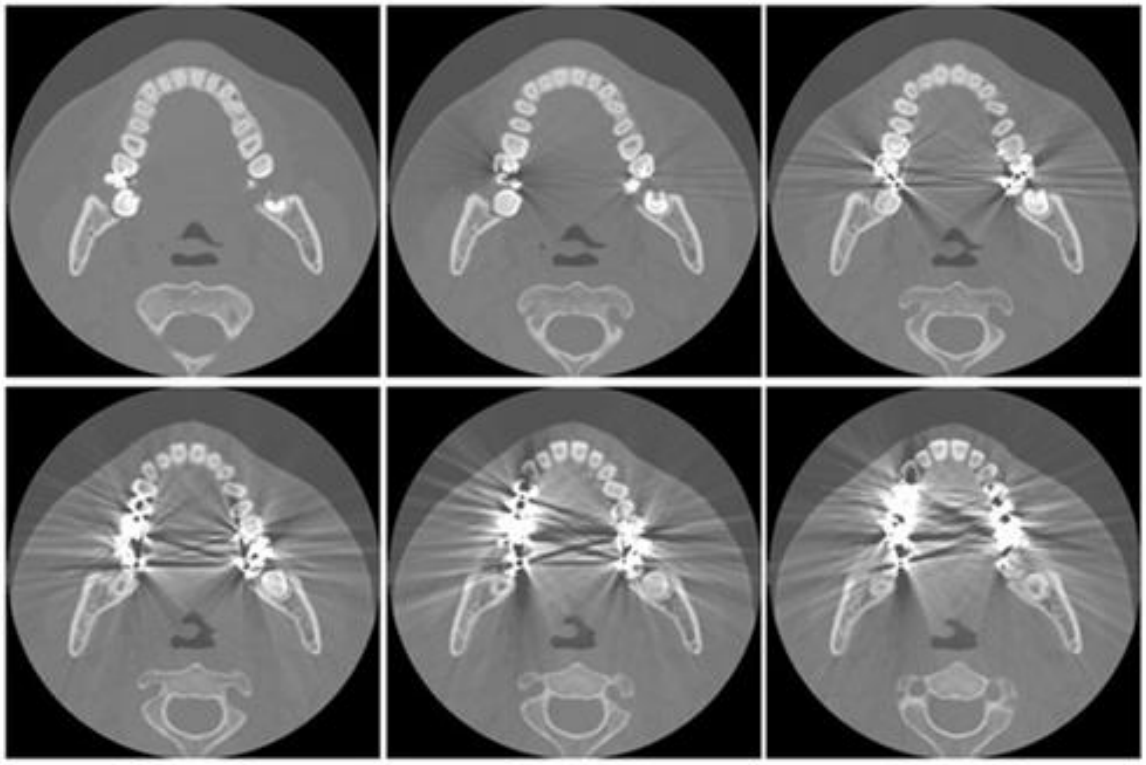

Fig.6.1 Continuous six original (unprocessed) maxilla slices. They are aligned from head to foot. The slices were obtained before the jaw deformity treatment operation.

Images shown from Fig.6.1 to Fig.6.6 are from a jaw deformity (mandibular retraction) case. Images shown in Fig.6.1 are original images. They were acquired as the pre-operative evaluation of bone morphology in the mandible for jaw deformity treatment. No orthodontic devices or titanium plates were present. Fig.6.2 is an artifact-free image, which is the adjacent image to the far left one in the top row in Fig.6.1. Its projection data (sinogram) is illustrated on the right.

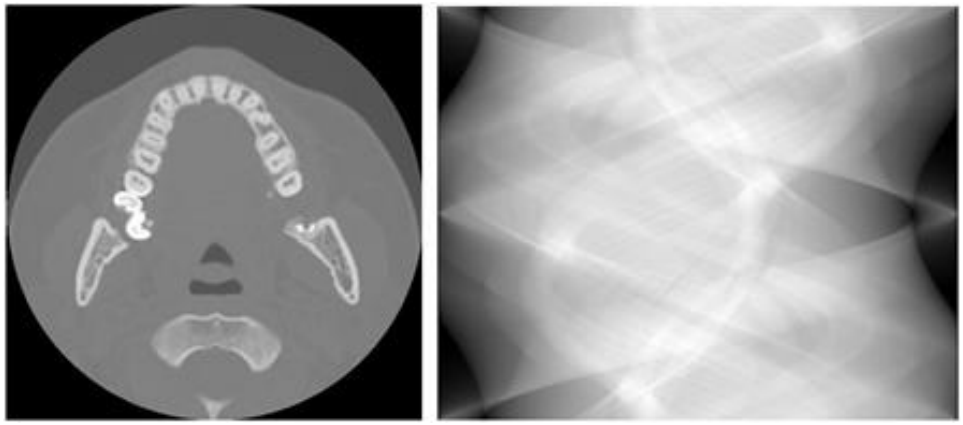

Fig.6.2 An artifact-free image with the projection data to its right. The artifact-free image is the adjacent image to the far left one in the top row of Fig.6.1.

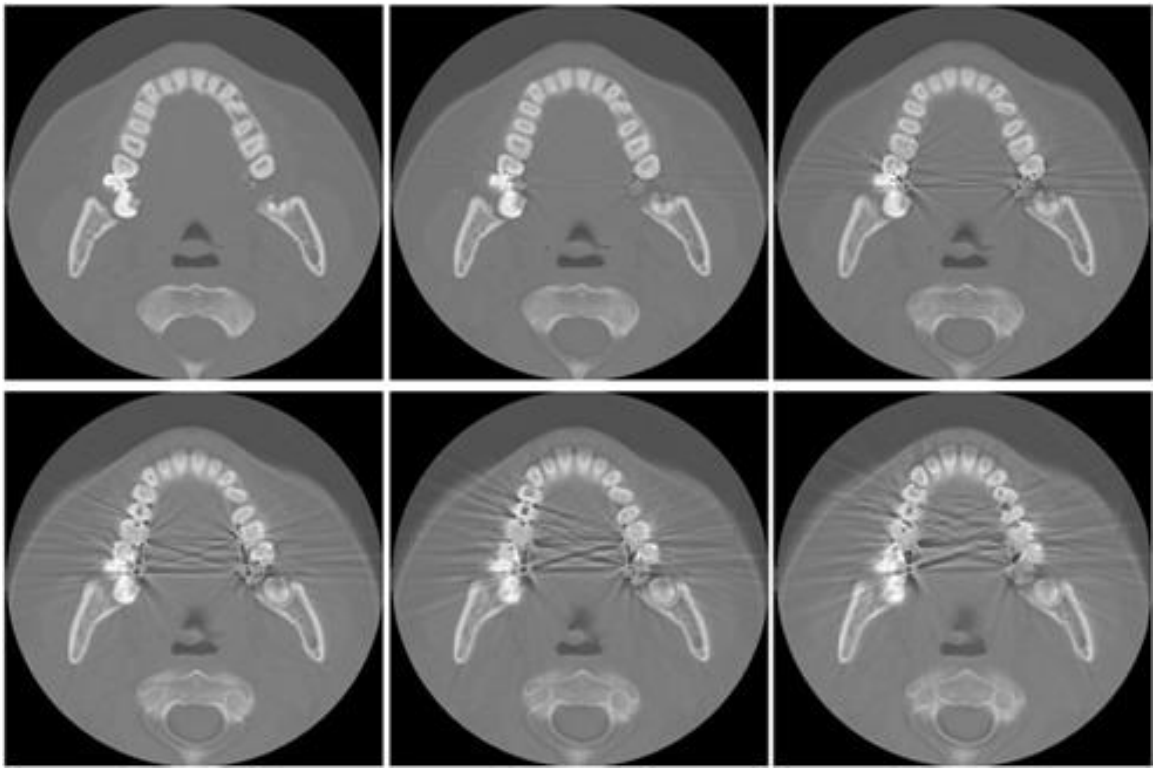

Fig.6.3 Resultant images processed by successive iterative OS-EM algorithm.

As indicated in Chapter V, the OS-EM successive iterative restoration algorithm was applied on images. The resultant images are shown in Fig.6.3, and they correspond to the order of images shown in Fig.6.1. On the original images in Fig.6.1, streak artifacts occurred from several tooth crown metallic restorations. Processing substantially reduced the streak artifacts (Fig.6.3).

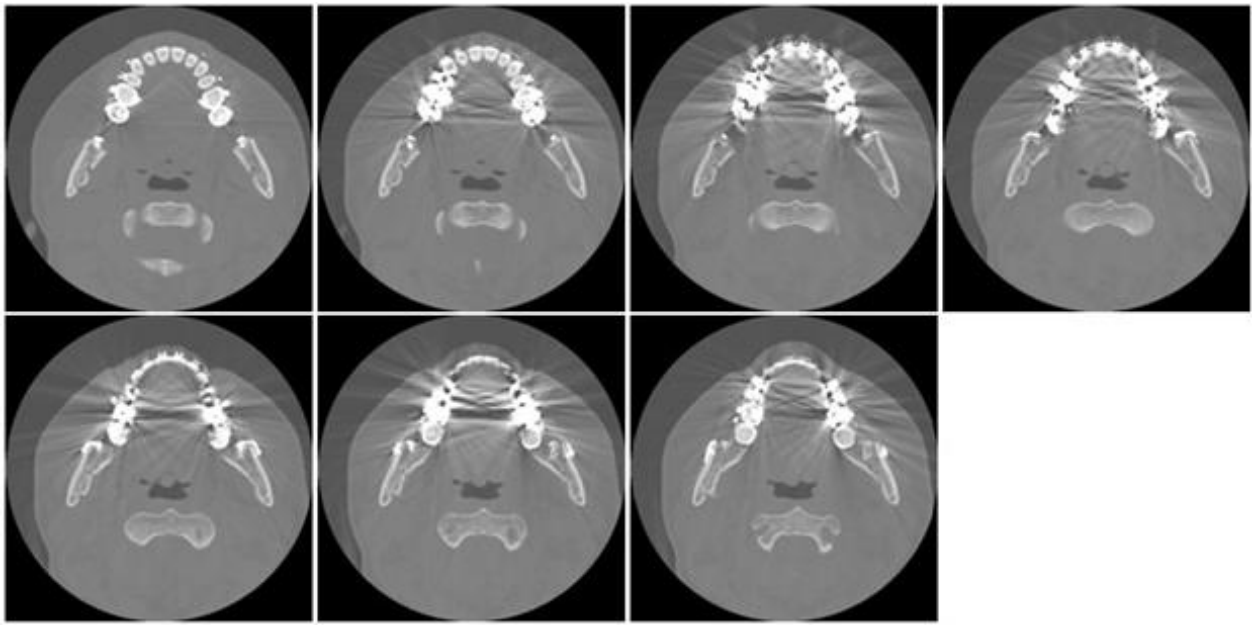

Fig.6.4 Continuous seven original (unprocessed) maxilla slices from head to foot. The image volume was obtained after surgery. The orthodontic wire and brackets, bone screws or titanium plates can be observed on some specific CT slices.

After receiving three years of orthodontic treatment, the patient had a surgical operation, using a sagittal split ramus osteotomy (SSRO). The CT images shown in Fig.6.4 were scanned for the post-operative diagnosis. The orthodontic wire and brackets, bone screws or titanium plates can be observed on some specific CT slices. The image in Fig.6.5 is an artifact-free image, which is attached with the projection data (sinogram), and it is the adjacent image to the far left one in the top row of Fig.6.5. As explained in Chapter V, the OS-EM successive iterative restoration algorithm was applied. The resultant images are shown in Fig.6.6, and they correspond to the order of images shown in Fig.6.4.

The original images in Fig.6.4 show streak artifacts which were intense. The artifacts were caused not only by dental restorative materials but also by the orthodontic wire, brackets and titanium plates. On the resultant images in Fig.6.6, streak artifacts caused by every kind of metallic materials were reduced effectively. Tooth shape reverted to the original states on the former images, while some false anatomical structures occurred in the incisor and cuspid areas on the latter images.

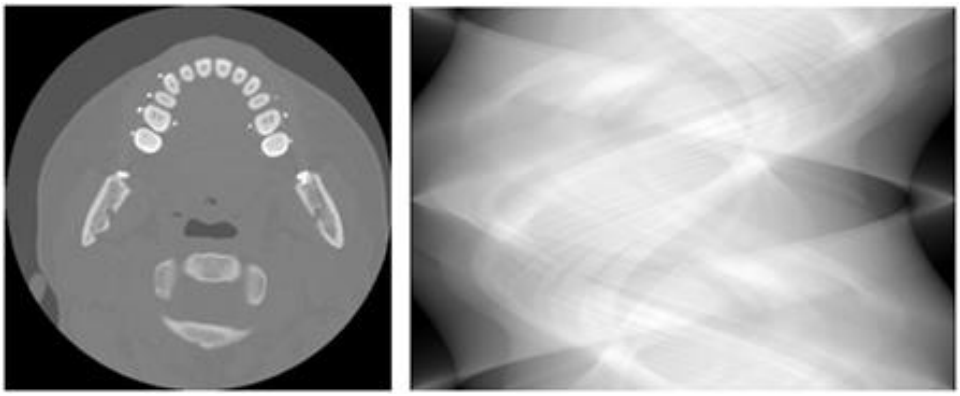

Fig.6.5 An artifact-free image and its projection data. The artifact-free image is the adjacent image to the far left one in the top row of Fig.6.4.

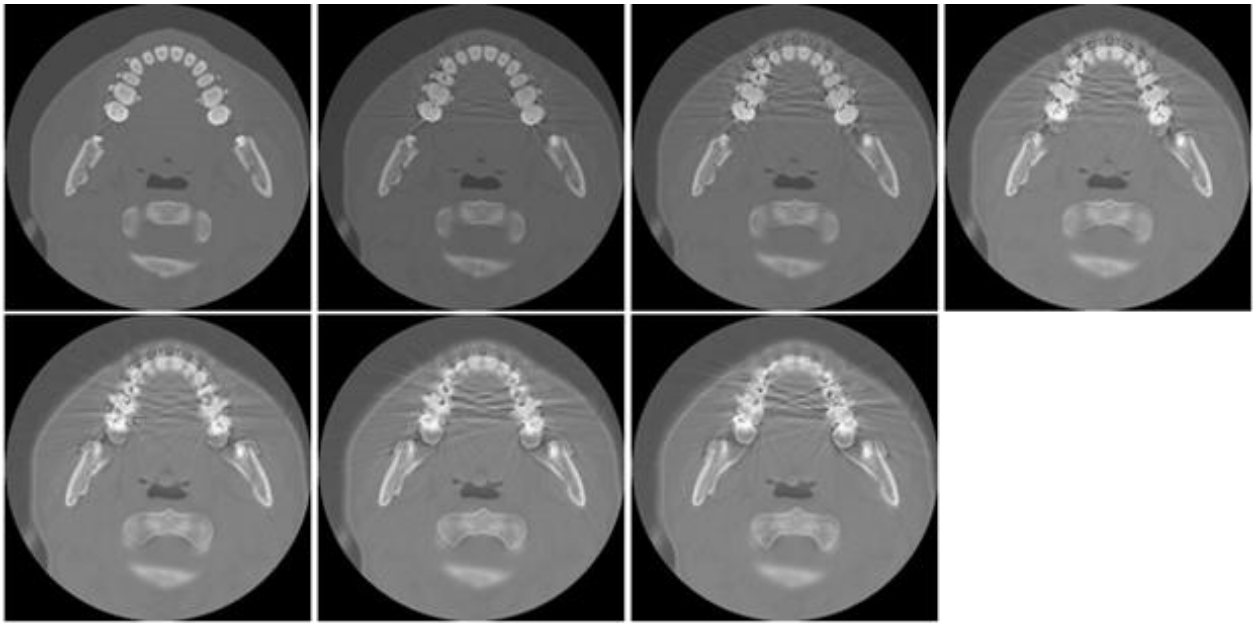

Fig.6.6 Reconstructed images by successive iterative OS-EM algorithm. They correspond to the seven images in Fig.6.4.

In addition, we reconstructed three-dimensional (3D) images using images from

Fig.6.4 and Fig.6.6. The OsiriX, 3D medical and photographic digital imaging and communications in medicine viewer, was used. The resulting 3D images are shown in Fig.6.7, and they represented only a thin part of the maxilla. The left and middle images in Fig.6.7 were merged, respectively, from slices where the streak artifacts appeared (Fig.6.4) and were reduced (Fig.6.6). The image on the right of Fig.6.7 presented a simultaneous visualization of the left and middle images with different colors. The difference of streak artifact appearances can be obviously recognized by viewing 3D images in Fig.6.7.

Fig.6.7 Volume-rendered images of maxilla. The left image is reconstructed by merging ten sequential multi-detector row CT slices from Fig.6.4. These are before streak artifact reduction. The middle one is reconstructed by merging ten MDCT slices from Fig.6.6. These are following streak artifact reduction. Superimposing of volume-rendered images are used to compare the 3D renderings before and after artifact reduction (image on the right).

Irregular artifacts, which were caused by the orthodontic wire and brackets, were observed at specific CT slices. Then, we applied a very small ROI setting segmented from original images No.1 to No.4 of Fig.6.4. The small ROI original images are shown in Fig.6.8. The No.3 and No.4 images contain too heavy streak artifacts that the anatomical structure is destroyed largely. The image in Fig.6.9 is an artifact-free image, which is attached with the projection data (sinogram). It is the adjacent image to the far left one in Fig.6.8. As explained in Chapter V, the

OS-EM successive iterative restoration algorithm was applied on segmented images. Resultant images are shown in Fig.6.10, and they correspond to the order of Fig.6.8. Because of the decreasing calculation loading, the processing duration time reduced to 10.4 s for reconstructing a single small ROI setting image, while it was 84 s for a single original-sized CT slice. In the original ROI images, streak artifacts seriously damaged the image quality, and on the resultant images in Fig.6.10, the tooth shape reverted to its original state clearly and streak artifacts were also reduced effectively for both teeth and soft tissues.

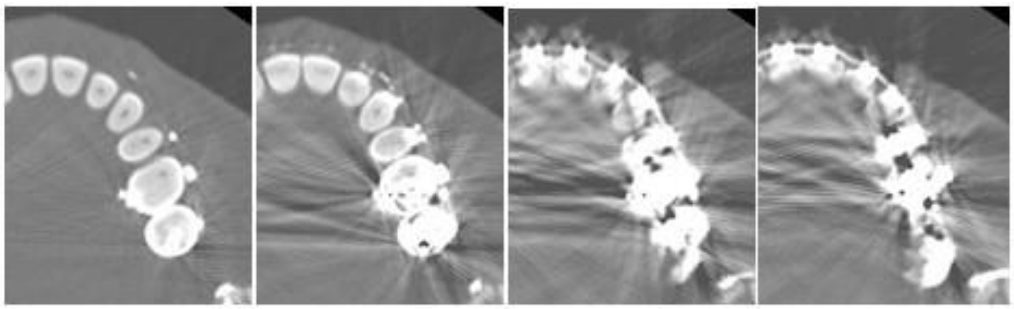

Fig.6.8 Region of interest (ROI) images of sequential images No.1 to No.4 in Fig.6.4. A part of the left mandible was segmented as a small ROI. These are original images without processing. The pixel matrix for the ROI images is 166 x 196.

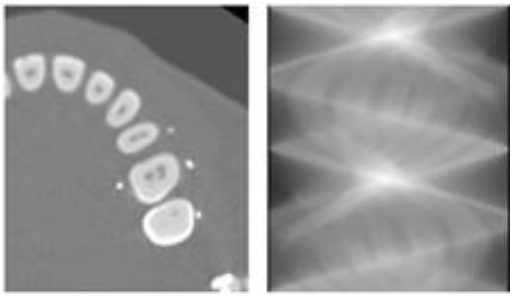

Fig.6.9 An artifact-free small region of interest setting image. This was segmented from the artifact-free image of Fig.6.5.

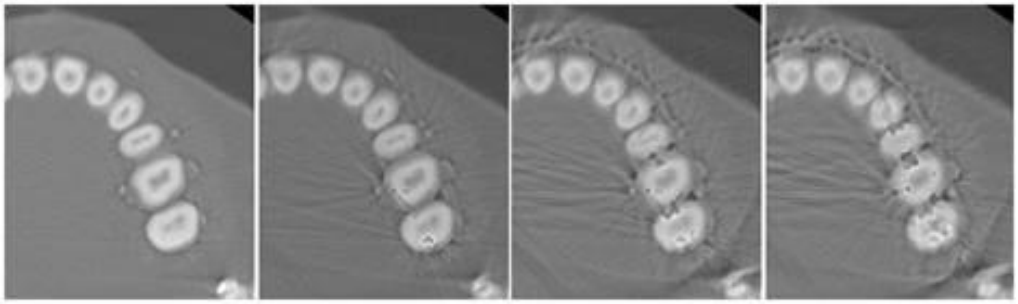

Fig.6.10 The reconstructed region of interest images by successive iterative OS-EM algorithm, corresponding in order to the sequence of images in Fig.6.8.

6.2 CUDA programming for GPGPU machine

General-purpose graphic processing unit (GPGPU) machine was originally used in the field of astronomical calculation. As a beginning for using in the field, general purpose GPU computing is attempted to be used in many fields and one of them is medical image processing. The high calculus ability and a reasonable price make the GPGPU computing a trend to improve the execution efficiency [22, 28].

In this study we used a high performance GPGPU machine to execute the streak artifact reduction algorithm. Three compute unified device architecture (CUDA) supporting GPUs, NVIDIA GeForce® GTX 680 (Santa Clara, CA), were installed. The programming language we used was CUDA. The CUDA program consists of CPU-driving host code and GPU-driving device code. A kernel function in the device code can divide a process to synchronous multi threads and the function is the most important part in CUDA codes.

Table 6.1 The computational loading comparison concerned with different algorithms and GPGPU runtime environment

Successive iterative restoration	*Execution parameters*	*Processing time*
ML-EM	50 times iteration	6 min 10 s
OS-EM	8 subsets / 10 times iteration	1 min 24 s
OS-EM on GPGPU	8 subsets / 10 times iteration	20 s

According to the steps of successive iterative OS-EM algorithms, the procedure of calculating projection data was repetitively executed for iteration times, while which was just the time consuming procedure because of enormous circulated

calculation. We divided up the projection data calculating procedure to synchronous multi threads according to projection acquisition angles. As a result, the execution time was largely reduced compared to that of not using GPGPU. We provided the computational loading comparison table in Table 6.1. It demonstrated that diving up the procedure with a large amount of calculating using CUDA language is an effective means for reducing processing time.

Chapter VII. Cone beam computed tomography image processing in dental office

7.1 Cone beam computed tomography

CBCT images has become increasingly important in treatment planning and diagnosis in dentistry of endodontics or orthodontics [33, 34]. CBCT systems are a variation of traditional CT system. The CBCT systems used by dental professionals rotate around the patient, capturing data using a cone-shaped X-ray beam. These data are used to reconstruct a three-dimensional image of the following regions of the patient's anatomy: dental (teeth); oral and maxillofacial region (mouth, jaw, and neck); and ears, nose, and throat.

X-ray imaging, including dental CBCT, provides a fast, non-invasive way of answering a number of clinical questions. Dental CBCT images could provide three-dimensional information. And this may help with the diagnosis, treatment planning and evaluation of certain conditions. Although the radiation doses from dental CBCT exams are generally lower than other CT exams, dental CBCT exams typically deliver more radiation than conventional dental X-ray exams.

In comparison with MDCT images, CBCT resolution is usually limited by the high noise due to the lower level of exposure in addition to the contrast resolution [35, 36]. Also since the usage of metallic prosthetic appliances, appearance of streak artifact is not avoidable, which makes images unusable for diagnostic purpose [37, 38]. Therefore, to improve the accuracy of bone morphology depicted in CBCT images, several attempts, including streak artifact reduction, three-dimensional filtering methods, and region growing method with dilation and erosion, have been performed in this chapter. The processes are designated to improve the CBCT image quality.

7.2 SIRM used in CBCT images for streak artifact reduction

Streak artifacts are usually caused by metallic prosthetic appliances, dental fillings or other metallic biomaterials. However, these metallic materials are predicted to be used for a long time in dento-alveolar region. In addition, because the soft-tissue contrast is usually lower in CBCT images, the impact of metal artifacts in the soft-tissue region is usually magnified. Thus streak artifact reduction in X-ray CBCT images is still a challenge. We have proposed successive iterative reconstruction algorithms in the previous chapter. They were maximum likelihood-expectation maximization (ML-EM) algorithm and Ordered subset-expectation maximization (OS-EM) algorithm. Both the two successive statistical iterative methods were proved to be effective to reduce streak artifacts in dento-alveolar region of X-ray MDCT images [20-22]. In addition, OS-EM algorithm was a time-saving and more efficient method in performance. In this section, we attempt to apply the successive iterative OS-EM reconstruction algorithm to reduce the streak artifact in CBCT images.

CBCT examination was performed using CB Throne (Hitachi Medical Systems, Tokyo, Japan). Principal exposure parameters were as follows: I-mode, filed of view (FOV) 10 cm in diameter, 120 kV, 15 mA, 0.2 mm slice thickness, and 10 s exposure time. The isotropic voxels were 0.2 x 0.2 x 0.2 mm, and the individual image matrix was 512 x 512 x 512. The images were a clinical case of Mucocele in the maxillary sinus. Since the application of dental fillings, metal-induced streak artifacts appeared. It covered depiction of anatomical structure and influenced effect of diagnosis. 16 continuous streak artifact containing slices are presented in Fig.7.1.

The CBCT slices have the thin thickness of 0.2 mm, which makes the adjacent slices depict very similar anatomical structures. Besides, there are artifact-free slices next to slices with heavy streak artifacts. We thus employed the successive

iterative restoration method. First the projection data of the artifact-free slice was obtained. The adjacent slice, which showed weak artifacts, was processed using the obtained projection data. We furthermore obtained the projection data of the processed image and used it to reconstruct the adjacent slice which contained a little more streak artifact. We did similar procedure until heavy streak artifacts image was processed. In this section, we chose OS-EM algorithm and the optimal parameters combination, subset = 8 and iteration = 10.

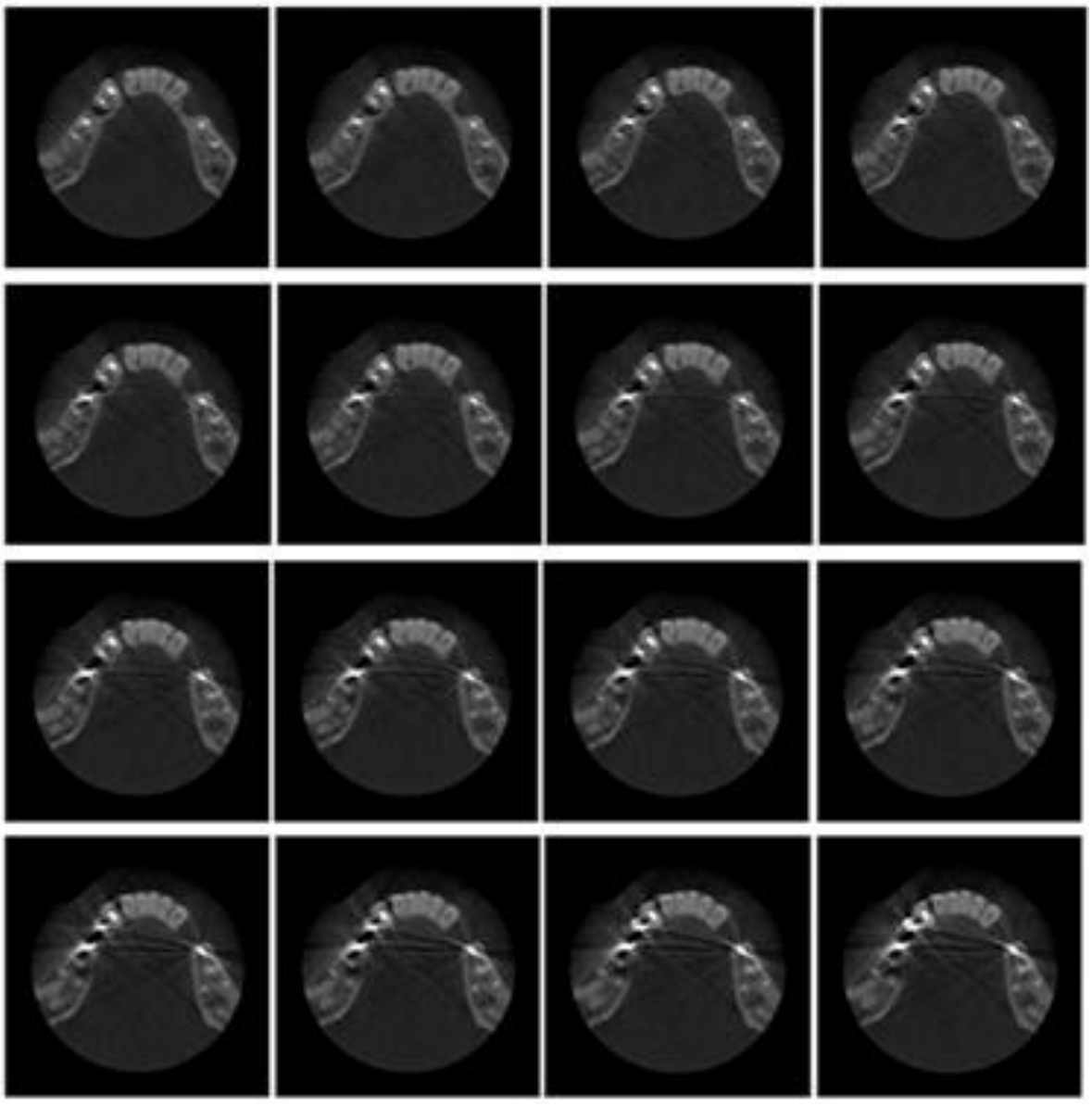

Fig.7.1 Sixteen continuous CBCT slices before artifact reduction

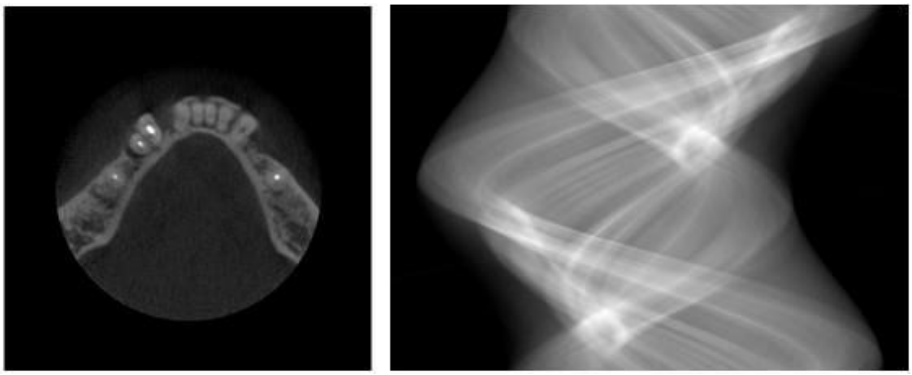

Fig.7.2 The artifact-free image (matrix 512 x 512), which is next to the image No.1 of Fig.7.1, and the projection data (matrix 512 x 360) computed from the artifact-free image.

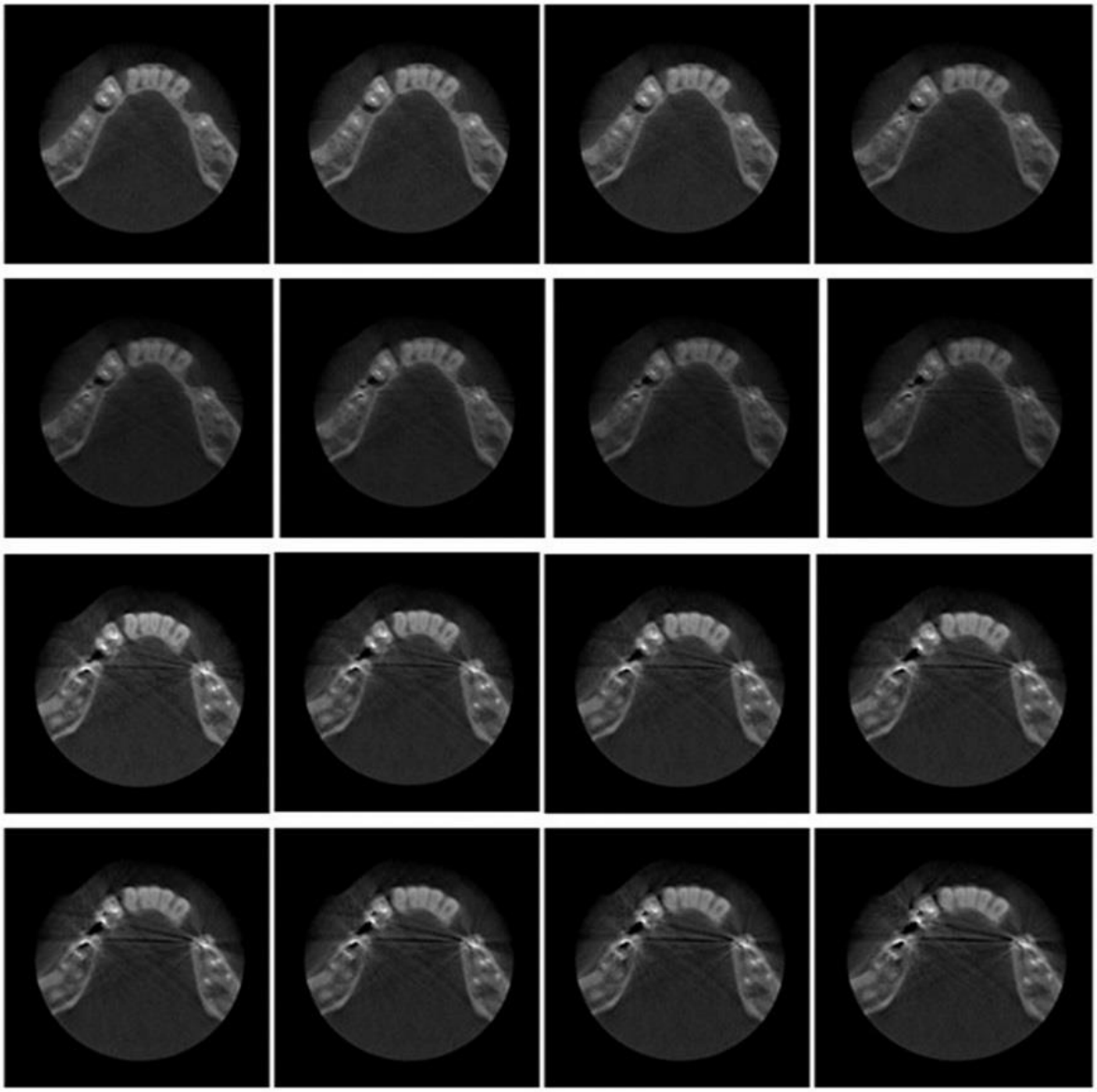

Fig.7.3 The reconstructed 16 images by successive iterative OS-EM reconstruction algorithm. They correspond to the order of Fig.7.1.

An artifact-free slice which is next to Image No.1 in Fig.7.1, and its projection data are presented in Fig.7.2. The projection data was acquired at 360 directions with 1 degree intervals. Continuous 16 processed images are presented in Fig.7.3. They correspond to the order of Fig.7.1. Streak artifacts were reduced obviously on the light artifact containing slices. However, some artifacts still remained on the heavy artifact containing images.

This is the first time that we used successive iterative reconstruction method to reduce metal-induced streak artifacts on CBCT images. Since the metal-induced artifacts were obvious in the low contrast soft-tissue region, the method did not work so effectively compared to MDCT image result. Some streak artifacts still remained on the heavy artifacts containing images. Moreover, the processed CBCT images have a gradually increasing field of view and it caused some deviation on the edge part of anatomical structure on each image.

7.3 3D Gaussian-Laplacian filtering method

To improve the image quality of CBCT images, the single procedure of streak artifact reduction is inadequate. One method to improve the depiction accuracy of CBCT images is digital filtering as a post-acquisition procedure. The filtering procedure generally involves image transformation in which the output image is weighted for a specific goal. Filtering is an image-processing procedure using specific local operators, which are sometimes called local matrices. Such processing procedures are useful for image sharpening, smoothing, edge detection, edge enhancement, etc [31, 36, 39].

For CBCT images, the filtering procedure can be applied not only on the 2D level (CBCT slices), but also can be applied on the 3D level (three-dimensional data file). The effectiveness of image quality improvement by 2D and 3D filtering should be

investigated. In section 7.3.1, 2D and 3D filtering methods were compared on CBCT images. Multi-planar reconstruction (MPR) image was used to show the different results of 2D and 3D filtering methods.

7.3.1 Comparison of 2D and 3D filtering methods

The 2D and 3D filtering procedures of averaging, median smoothing, and Gaussian smoothing were compared. For further comparison, Gaussian smoothing followed by Laplacian sharpening was also applied.

When 2D functions f(x, y) and g(x, y) are defined as input and output images, respectively, 2D filtering procedures are expressed as follows:

$$g(x,y) = \sum_{k=-M/2}^{M/2} \sum_{l=-N/2}^{N/2} f(x+k, y+l)h(k,l)$$

The function h (k, l) is a spatial filter (or local operator) with matrix size M x N. Parameters x and y are variables to indicate the pixel at the center of the spatial filter.

Similarly, the 3D filtering procedure is expressed as follows:

$$g(x,y,z) = \sum_{i=-L/2}^{L/2} \sum_{j=-M/2}^{M/2} \sum_{k=-N/2}^{N/2} f(x+i, y+j, z+k)h(i,j,k)$$

where f(x, y, z) and g(x, y, z) are input and output images in three dimension; h(i, j, k) is a spatial filter (or local operator); and the matrix size is L x M x N. x, y, z are variables to indicate the voxel at the center of the spatial filter.

Because of the concept of the neighbor pixels (or voxels), two alternatives exist for the filtering procedures in 2D and 3D, respectively [35]. As shown in Fig.7.4, two alternatives are possible in the numbers of neighboring pixel (or voxels) to be incorporated into the calculation; 4 neighbors or 8 neighbors in 2D filtering and 6 neighbors or 26 neighbors in 3D filtering. Only 8 neighbors in 2D and 26 neighbors in 3D were examined in this section.

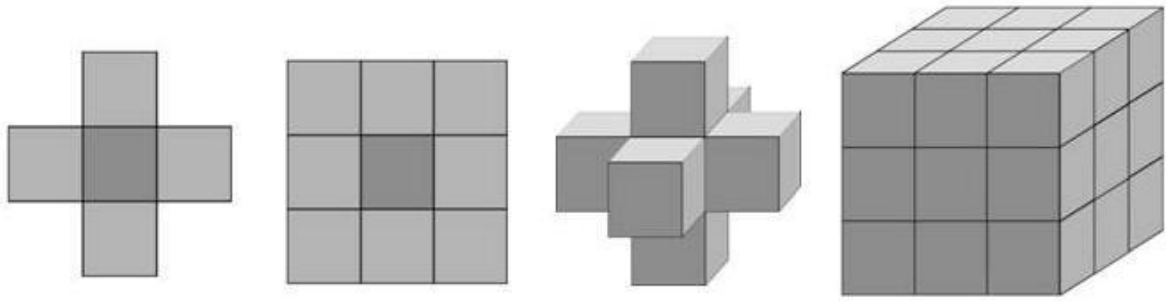

Fig.7.4 Two alternative matrices for filtering in 2D and 3D, respectively. In this section, only 8 neighbors in 2D and 26 neighbors in 3D were examined. The image data is from Sagawa's paper (Ref.34).

The details of the filtering procedures are as follows:

1. Averaging: all 9 pixels (the center pixel and 8 neighbors) in 2D and 27 voxels (the center voxel and 26 neighbors) in 3D have uniform weighting.
2. Median smoothing: the value of the center pixel (or voxel) is replaced with the median value of 9 pixels and 27 voxels.
3. Gaussian smoothing: according to the Gaussian function, weighting factors are changed between the center pixel (or voxel) and neighbors.
4. Laplacian sharpening: the weighing factors are set at -1 for all neighbors. The weighting factors at the center pixel and voxel are 9 and 27, respectively.

Effects of each filtering procedures were examined by the MPR images. The original image and processed images at the mid-sagittal plane are presented in Fig.7.5. The processed images in the array show averaging, median smoothing, Gaussian smoothing [sigma, standard deviation, was set at 2.0 (σ =2.0)], and the Laplacian sharpening preprocessed by the Gaussian smoothing from the second row to the lowest row. Images processed by 2D filters are shown on the left, and those by 3D filters are shown on the right.

Each image shows the grayscale profile along a specific vertical line, which is indicated by a vertical line and arrows. Line profiles show gray level distributions of corresponding pixels in each image. Similar profiles appeared on the first three

images. But profiles showed difference between 2D and 3D in Gaussian-Laplacian processing images. The 3D processed images depicted clearer anatomical structure than 2D processed images. The difference between 2D and 3D filtering procedures was thought to appear along the superior-inferior (S-I) direction.

By analyzing the result images, the most effective filtering method can be concluded as the 3D Gaussian-Laplacian filter and we applied this 3D filter to artifact reduced CBCT images in the next section.

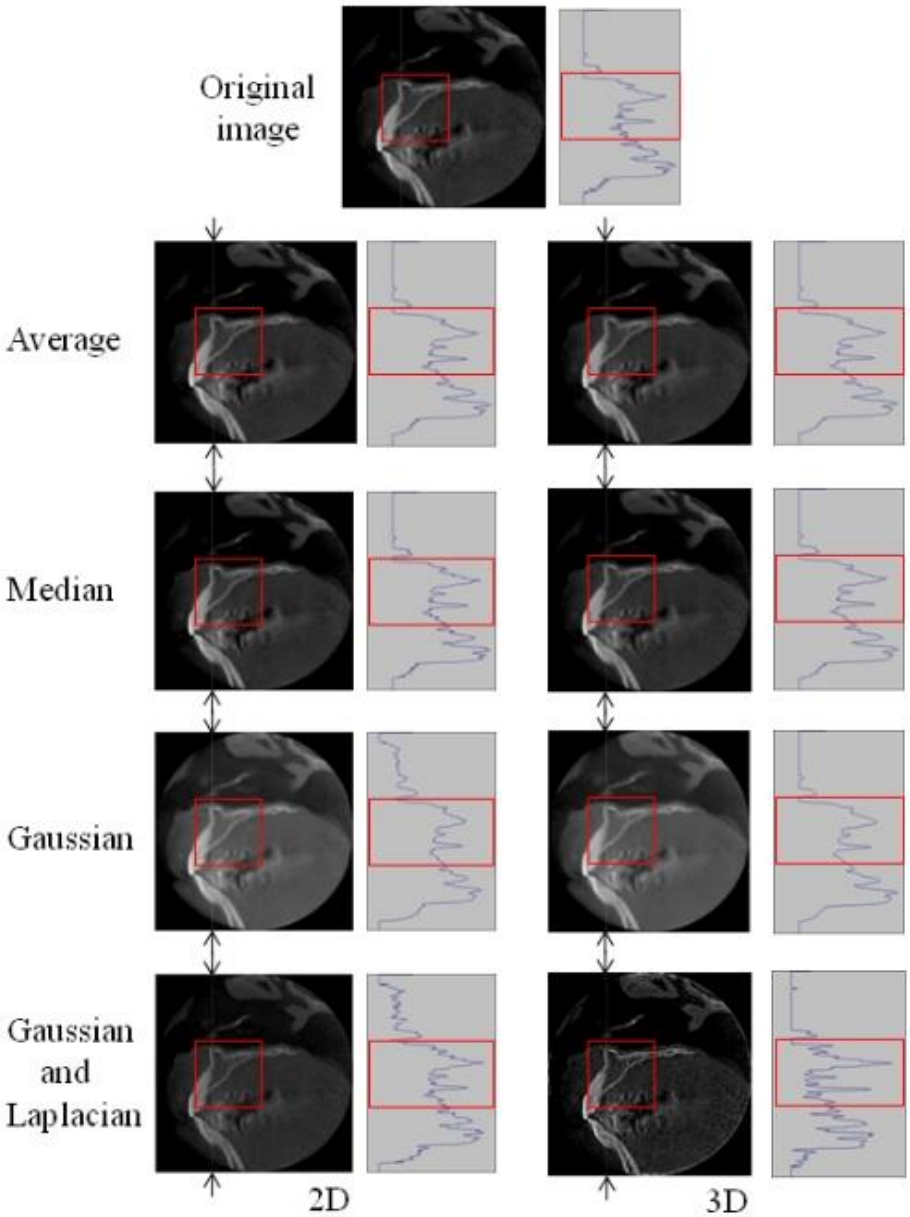

Fig.7.5 MPR images at mid-sagittal plane. The original image (top row) and processed images in the following. Profiles on a special line is shown on the right. The image data is from Sagawa's paper (Ref.34)

7.3.2 Apply 3D Gaussian-Laplacian filter on artifact reduced CBCT images

In section 7.3.1, Averaging, median smoothing, Gaussian smoothing, and Laplacian sharpening following Gaussian smoothing in 2D and 3D level were tested. Multi-planar reconstruction (MPR) images at the mid-sagittal plane on the maxilla were presented to examine the effect of each filtering. As the difference between 2D and 3D filtering procedures was thought to appear along the superior-inferior (S-I) direction, 3D filtering presented better results in improving accuracy of bone morphology. We thus decide to use the 3D Gaussian-Laplacian filtering procedure to artifact reduced CBCT images. The resulting CBCT images (streak artifact reduced images by successive iterative OS-EM reconstruction method) from section 7.2 are the processing objects in this section.

The formulation of 3D Gaussian-Laplacian filter is described as follows:

$$\nabla^2 G(x,y,z) = \frac{x^2+y^2+z^2-3\sigma^2}{\left(\sqrt{2\pi}\right)^3\sigma^7}\exp\left\{-\frac{x^2+y^2+z^2}{2\sigma^2}\right\}$$

The standard deviation σ in the formulation is a decisive factor of sharpening effect. Sharpening effect will be reduced as the value of σ increasing [30]. We set σ at 0.5 (σ =0.5), and filter radius at 2. The filter matrix is 5 x 5 x 5. Two set of multi-planar reconstruction images, left side molar plane and mid-sagittal plane, were presented to show the 3D digital filtering effect.

In Fig.7.6, left side molar plane (the left side) and mid-sagittal plane (the right side) images are presented to show the effects of OS-EM algorithm and Gaussian-Laplacian filtering method. The first row shows the original images. Images of streak artifact reduction by successive iterative OS-EM algorithm are on the second row. Images of Gaussian-Laplacian filter applying after streak artifact reduction are shown on the third row. Each image shows the grayscale profile along the specific vertical line, which is indicated by a vertical line and arrows.

Line profiles show gray level distributions of corresponding pixels in each image. The profiles showed differences in OS-EM processed area and Gaussian-Laplacian filtered images.

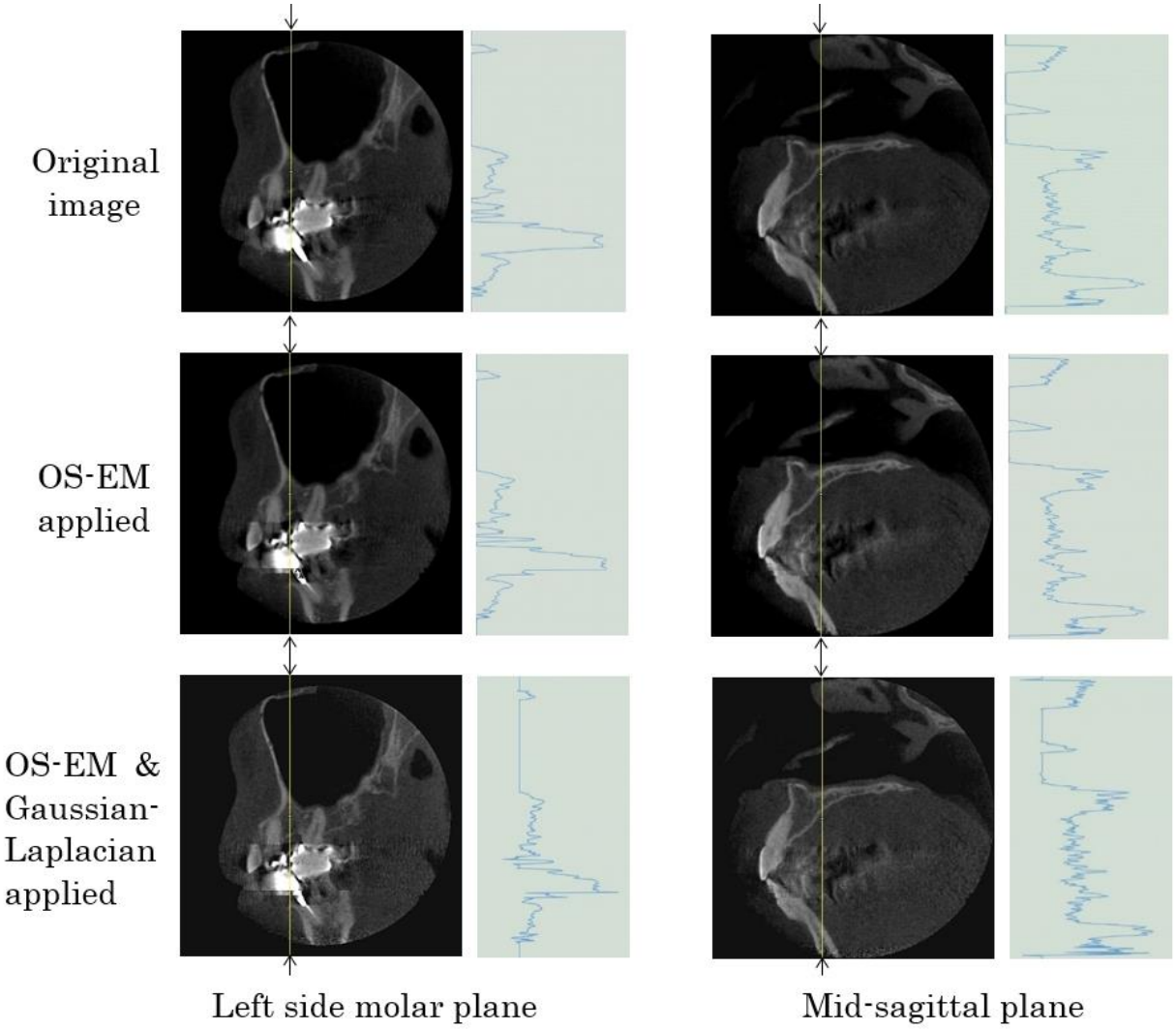

Fig.7.6 MPR images at left molar sagittal plane and mid-sagittal plane are presented. Images on the first row are from the original CBCT file. Images on the second row are from the OS-EM processed slices. And images on the third row are from the OS-EM and Gaussian-Laplacian filter processed slices. The grayscale profile along the specific vertical line indicated by arrows was attached to each image.

Since improvement of image quality was valued, 5 x 5 x 5 filter was examined. Images at left side molar plane and mid-sagittal plane were shown in Fig.7.6. Profiles of a special line were also presented. Differences between the profiles of

the same plane showed the effect of streak artifact reduction and image quality improvement by Gaussian-Laplacian filter. In this study, only the 5 x 5 x 5 filter was examined. The loading of the calculation was a little high and it required several minutes on our desktop PC.

7.4 Region growing for segmenting clear maxilla morphology

Region growing method is often used to segment special tissues from medical images [40, 41]. Firstly, region grow starting point is marked within the area of segmentation object. Then connected pixels are accessed based on segmentation conditions. The pixel will be sorted as segmentation area if it meets the condition. The process lasts until there is no qualified pixels. We performed region growing method to present the maxillofacial region in this section.

We performed 3D region growing method to segment maxillofacial region according to the following steps.

1. Select one voxel as the region growing starting point within the area of segmentation object.
2. If the selected voxel meets the segmentation condition, set value of the same coordinate voxel on the output image.
3. Add the neighboring voxels of the valued voxel to verifying list (26-nearest neighborhood voxels were examined).
4. Verify the voxels in the list, value them if they meet the segmentation condition. Back to step 3.
5. Perform the above steps until the list is null. Make sure that each voxel is verified only once.

There are usually depression or protrusion parts on the segmentation object after the above procedure [42, 43]. Further steps, dilation and erosion, were taken

for enhancement. Fig.7.7 showed the dilation and erosion procedure and it is also called closing processing.

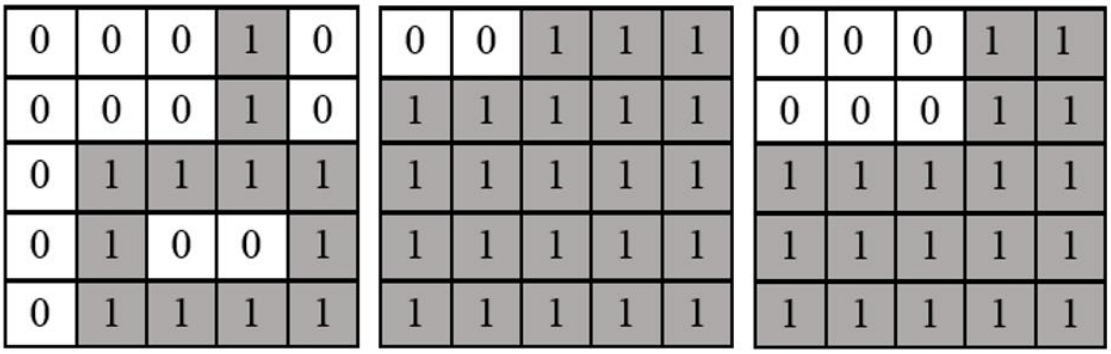

Fig.7.7 An example of closing procedure. They are original data, dilation procedure and erosion procedure from left to right.

To obtain clear anatomical structure from CBCT slices, we performed region growing method on three dimensional CBCT image, and further more we applied dilation and erosion procedures after region growing processing. We presented 2D and 3D resultant images in Fig.7.8. The images on the top row are 2D level images, and the images on the bottom row are 3D level images. The original CBCT images are shown in the first column. Images processed by region growing method are shown in the second column. We set starting point at voxel (252,136,255). The resulting segmented image by single region growing method shows some blurring structures on both teeth and bone parts. And images processed by the dilation and erosion processing after region growing method are shown in the third column. The anatomical structure became clearer. After each processing, images showed differences in visualization of maxillofacial region.

Region growing method with dilation and erosion provided clearer maxillofacial morphology than that with only region growing method. The dilation and erosion processing can remove the depression and protrusion parts on the segmented

image. However, the processing needed to check each voxel on the 3D file, which made the loading of the calculation higher.

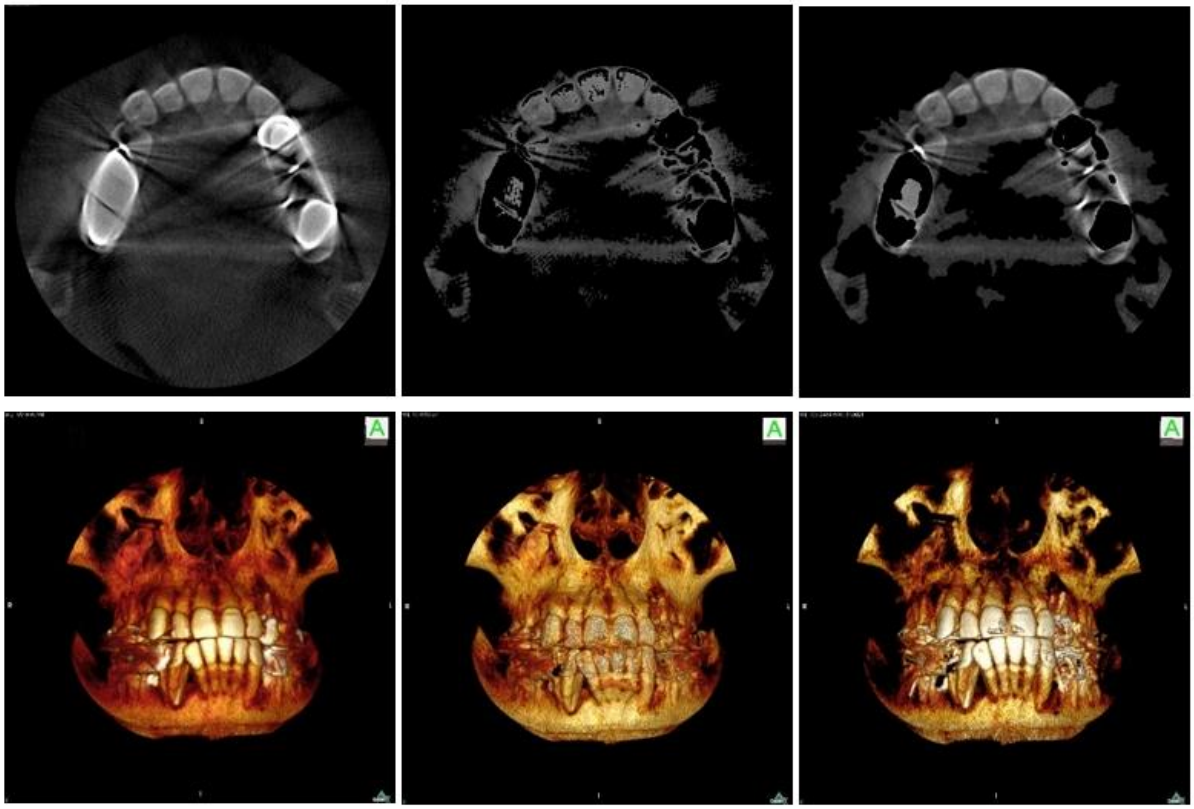

Fig.7.8 2D and 3D images of original CBCT file, only region growing file, and closing processing after region growing file respectively.

In conclusion, CBCT images are composed of fine and isotropic voxels, but metal-induced streak artifacts and noise level are comparatively high due to the low exposure. In this chapter, successive iterative reconstruction method for streak artifact reduction was applied. Furthermore, 3D digital filter for noise reduction and region growing method for clear morphology segmentation were also performed. We validated the improvement of image quality by creating the grayscale profile of MPR image before and after the mentioned processes. We realized the image quality improvement of 3D CBCT by these approaches.

Chapter VIII Research summary and conclusion

When metallic prosthetic appliances and dental fillings exist in the oral cavity, the appearance of metal-induced streak artifacts is not avoidable in CT images. The general objective of this research work was to reduce the metal-induced streak artifacts using successive iterative reconstruction method. ML-EM and OS-EM algorithms were analyzed and used in this study. Besides streak artifact reduction, 3D filtering method and region growing method were applied to improve image quality.

8.1 Research summary

In Chapter I, discipline of medical imaging was introduced. Among several medical imaging modalities, X-ray CT was emphatically introduced from its tomography principles to its application. Artifacts which were usually observed on CT images were analyzed and sorted to several kinds. Although the traditional CT reconstruction method, the FBP algorithm, had been widely applied, it could not deal with the loss of portions on projection data which was caused by extremely high X-ray absorption coefficients of metallic biomaterials. Image reconstruction algorithms that can use the corrupted projection data were expected.

In Chapter II, the regularly used image format, DICOM, was introduced firstly. It is the abbreviation of digital imaging and communication in medicine. Fundamental composition of DICOM images was expressed. Special information about patient and examination are contained in DICOM images. Image size, bits allocation were analyzed subsequently. Two medical image displaying software, Image J and OsiriX, were introduced. We used Image J to display and analyze 2D images. We used OsiriX to present 3D volume rendering.

In Chapter III, projection data acquisition on X-ray CT modality was instructed

in detail. All the projection data were acquired in 360 directions with 1 degree intervals in this study. Then, iterative restoration methods as CT image reconstruction algorithms, ML-EM and OS-EM, were proposed. The two algorithms both result in an approximation between the processing image and the target image.

A 3 × 3 matrix reconstruction by ML-EM algorithm was simulated. It simply demonstrated the image reconstruction process. Only 26 iterative calculations reached the target matrix. However, much more iterations were estimated to be needed for reconstructing 512 × 512 CT images. Subsequently, convergence validation of both ML-EM and OS-EM algorithms were carried out on practical images. It can be concluded that almost 300 iterations were needed to reconstruct the practical image by ML-EM, while the iteration times was about 50 for OS-EM algorithm to reconstruct the same image. The OS-EM algorithm can reconstruct image data faster without image quality dropped and it is usually used to reduce the calculation time.

In Chapter IV, variable optimization of ML-EM algorithm was tested when using in streak artifact reduction. 50 iterations could reach a best artifact reduction effect. More than 50 iterations could not improve the effect any more. Then we applied the ML-EM on a sequential CT images to reduce artifacts using the same artifact-free image's projection data. For OS-EM algorithm, the best parameter combination was proved to be subset = 8 and iteration = 10.

In Chapter V, we proposed the successive iterative reconstruction method (SIRM) based on the fact that adjacent CT images often depict very similar anatomical structures within the resulting collection of thin-slice images. We used SIRM in streak artifact reduction in dento-alveolar region. First the projection data of the artifact-free slice was obtained. The adjacent slice, which showed weak

artifacts, was processed using the artifact-free slice's projection data. Then the projection data of the newly processed image was obtained and it was used to reconstruct the next image which contained a little more artifacts. In this manner, the processing continued until the heave streak artifact containing image was processed. Two alternative algorithms were tested in processing sequential images for artifact reduction with SIRM.

In Chapter VI, SIRM was clinically applied in streak artifact reduction. Images before and after sagittal split ramus osteotomy operation (a jaw deformity case) were processed. The method was also proved to be effective in reducing artifacts caused by orthodontic wire, brackets, bone screws or titanium plates. Calculation acceleration was realized by general purpose graphic processing unit (GPGPU).

In Chapter VII, SIRM was applied in cone-beam CT images for streak artifact reduction. Cone-beam CT has become increasingly important in treatment planning and diagnosis in dentistry of endodontics or orthodontics. Besides, 3D filtering method and region growing method with dilation and erosion were employed for image quality improvement.

8.2 Conclusion

The dissertation has presented a better solution for metal-induced streak artifacts reduction in X-ray CT images. ML-EM and OS-EM algorithm were both proved to be effective in artifacts reduction. Successive iterative reconstruction method reduced the deviations on edge of anatomical structure. GPGPU processing realized the calculation acceleration. Image quality improvement was also realized in three dimensional level.

References

1. Fleischmann D, Boas FE. Computed tomography—old ideas and new technology. Eur Radiol 2011; 21: 510–17.
2. Silva AC, Lawder HJ, Hara A, Kujak J, Pavlicek W. Innovations in CT dose reduction strategy: application of the adaptive statistical iterative reconstruction algorithm. AJR Am J Roentgenol 2010; 194: 191–9.
3. Kubo T, Lin PJP, Stiller W, Takahashi M, Kauczor HU, Ohno Y, et al. Radiation dose reduction in chest CT: a review. Am J Roentgenol. 2008;190:335–43.
4. Pan X, Sidky EY, Vannier M. Why do commercial CT scanners still employ traditional, filtered back-projection for image reconstruction? Inverse Probl 2009; 25: 1230009. doi: 10.1088/0266-5611/25/12/123009
5. Imai K, Ikeda M, Enchi Y, Niimi T. Quantitative assessment of image noise and streak artifact on CT image: comparison of z-axis automatic tube current modulation technique with fixed tube current technique. Comput Med Imaging Graph 2009; 33:353-358.
6. Shimamoto H, Kakimoto N, Fujino K, Hamada S, Shimosegawa E, Murakami S, Furukawa S, Hatazawa J. Metallic artifacts caused by dental metal prostheses on PET images: a PET/CT phantom study using different PET/CT scanners. Ann Nucl Med 2009; 23: 443-449.
7. Prell D, Kyriakou Y, Beister M, Kalender WA. A novel forward projection-based metal artifact reduction method for flat-detector computed tomography. Phys Med Biol 2009;54:6575-6591.
8. Meyer E, Raupach R, Lell M, Schmidt B, Kachelriess M. Normalized metal artifact reduction (NMAR) in computed tomography. Med Phys 2010; 37: 5482-

93.

9. Rinkel J, Dillon WP, Funk T, Gould R, Prevrhal S. Computed tomographic metal artifact reduction for the detection and quantitation of small features near large metallic implants: a comparison of published methods. J Comput Assist Tomogr. 2008;32: 621–9.
10. Bal M, Spies L. Metal artifact reduction in CT using tissue-class modeling and adaptive prefiltering. Med Phys 2006;33:2852-2859.
11. Tohnak S, Mehnert AJ, Mahoney M, Crozier S. Dental CT metal artefact reduction based on sequential substitution. Dentomaxillofac Radiol 2011;40:184-90.
12. Rashed EA, Kudo H. Intensity-based Bayesian framework for image reconstruction from sparse projection data. Med Imaging Technol Jpn 2009;27:243-251.
13. Rashed EA, Kudo H. Statistical image reconstruction from limited projection data with intensity priors. Phys Med Biol 2012; 57: 2039–61.
14. Abdoli M, Ay MR, Ahmadian A, Dierckx RA, Zaidi H. Reduction of dental filling metallic artifacts in CT-based attenuation correction of PET data using weighted virtual sinograms optimized by a genetic algorithm. Med Phys 2010;37:6166-77.
15. Liu PT, Pavlicek WP, Peter MB, Spangehl MJ, Roberts CC, Paden RG. Metal artifact reduction image reconstruction algorithm for CT of implanted metal orthopedic devices: a work in progress. Skeletal Radiol 2009;38:797-802.
16. Joemai RM, de Bruin PW, Veldkamp WJ, Geleijns J. Metal artifact reduction for CT: development, implementation, and clinical comparison of a generic and a scanner-specific technique. Med Phys 2012;39:1125-32.
17. Ratib O, Rosset A. Open-source software in medical imaging: development of OsiriX. Int J Comput Assist Radiol Surg. 2006;1:187–96.

18. Beister M, Kolditz D, Kalender WA. Iterative reconstruction methods in X-ray CT. Phys Med 2012; 28(2):94-108.
19. Kondo A, Hayakawa Y, Dong J, Honda A. Iterative correction applied to streak artifact reduction in an X-ray computed tomography image of the dento-alveolar region. Oral Radiol 2010; 26: 61–5. doi: 10.1007/s11282-010-0037-6
20. Dong J, Kondo A, Abe K, Hayakawa Y. Successive iterative restoration applied to streak artifact reduction in X-ray CT image of dento-alveolar region. Int J Comput Assist Radiol Surg 2011; 6: 635–40. doi: 10.1007/s11548-010-0544-2
21. Dong J, Hayakawa Y, Kannenberg S, Kober C. Metal-induced streak artifact reduction using iterative reconstruction algorithms in x-ray computed tomography image of the dentoalveolar region. Oral Surg Oral Med Oral Pathol Oral Radiol 2013; 115: e63–73. doi: 10.1016/j.oooo.2012.07.436
22. Dong J, Hayakawa Y, Kober C. Statistical iterative reconstruction for streak artifact reduction when using multidetector CT to image the dento-alveolar structures. Dentomaxillofac Radiol, vol.43, issue 5, 20130373, June 2014.
23. Dong J, Kondo A, Tang WJ, Abe K, Hayakawa Y. ML-EM reconstruction algorithm applied to streak artifact reduction in X-ray CT image, International Workshop on Modern Science and Technology 2010 (IWMST2010), Proceedings, pp.138-140, Kitami, 2010.
24. Hwang D, Zeng GL. Convergence study of an accelerated ML-EM algorithm using bigger step size. Phys Med Biol. 2006; 51:237–52.
25. 董建，近藤篤，阿部恒介，早川吉彦，Sven Kannenberg，Cornelia Kober，OS-EM 画像再構成法を用いて X 線 CT 画像における金属アーチファクトの軽減，第 10 回情報科学技術フォーラム（FIT2011），第 2 分冊 pp.109-112, 2011.
26. Wang G, Frei T, Vannier MW. Fast iterative algorithm for metal artifact reduction in X-ray CT. Acad Radiol 2000;7:607-614.

27. Gutman F, Gardin I, Delahaye N, Rakotonirina H, Hitzel A, Manrique A, et al. Optimization of the OS-EM algorithm and comparison with FBP for image reconstruction on a dual-head camera: a phantom and a clinical 18F-FDG study. Eur J Nucl Med Mol Imaging 2003;30:1510-9.
28. Xu F, Xu W, Jones M, Keszthelyi B, Sedat J, Agard D, Mueller K. On the efficiency of iterative ordered subset reconstruction algorithms for acceleration on GPUs. Comput Methods Programs Biomed 2010;98:261-70.
29. Chen H, Lei X, Yao D. An improved ordered subsets expectation maximization positron emission computerized tomography reconstruction. Comput Biol Med. 2007;37(12):1780-85.
30. 董建，宮中大，張昕源，早川吉彦，歯顎顔面部コーンビーム CT の多断面再構成像における逐次近似法と 3 次元フィルタリングによる画質向上の検討，第 32 回日本医用画像工学会大会，Proceeding in CD-ROM，東京，2013.
31. Kubo T, Nishino M, Kino A, Yoshimura N, Lin PJ, Takahashi M, et al. 3-Dimensional adaptive raw-data filter: evaluation in low dose chest multidetector-row computed tomography. J Comput Assist Tomogr. 2006;30:933–8.
32. Bonciu C, Rezaee MR, Edwards W. Enhanced visualization methods for computed radiography images. J Digit Imaging. 2006 Jun;19(2):187-96.
33. Miracle AC, Mukherji SK. Cone beam CT of the head and neck, part2: clinical applications. AJNR Am J Neuroradiol 2009;30:1285-1292.
34. Arnheiter C, Scarfe WC, Farman AG. Trends in maxillofacial cone-beam computed tomography usage. Oral Radiol. 2006;22:80–5.
35. Sagawa M, Miyoseta Y, Hayakawa Y, Honda A. Comparison of two- and three-dimensional filtering methods to improve image quality in multiplanar reconstruction of cone-beam computed tomography. Oral Radiol. 2009;25:154-

58.

36. Kalra MK, Wittram C, Maher MM, Sharma A, Avinash GB, Karau K, et al. Can noise reduction filters improve low-radiation dose chest CT images? Pilot study. Radiology. 2003;228:257–64.

37. S. Kannenberg, J. Dong, A. Kondo, K. Abe, Y. Hayakawa, and C. Kober, Basic evaluation of artifact reducing algorithms for medical CT data, 情報処理北海道シンポジウム 2011, pp.213-214, 北見, 2011.

38. Boas FE, Fleischmann D. Evaluation of two iterative techniques for reducing metal artifacts in computed tomography. Radiology 2011;259:894-902.

39. Bal M, Spies L. Metal artifact reduction in CT using tissue-class modeling and adaptive prefiltering. Med Phys 2006;33:2852-9.

40. Shi H, Scarfe WC, Farman AG. Maxillary sinus 3D segmentation and reconstruction from cone beam CT data sets. Int J Comput Assist Radiol Surg. 2006;1:83–9.

41. Jiang H, He B, Fang D, Ma Z, Yang B, Zhang L. A region growing vessel segmentation algorithm based on spectrum information. Comput Math Methods Med. 2013;2013:743870.

42. Loubele M, Maes F, Schutyser F, Marchal G, Jacobs R, Suetens P. Assessment of bone segmentation quality of cone-beam CT versus multislice spiral CT: a pilot study. Oral Surg Oral Med Oral Pathol Oral Radiol Endod. 2006;102:225–34.

43. 相澤光博, 西川慶一, 佐々木啓太, 小林紀雄, 山満, 柿澤卓, 佐野司, 村上伸一. 歯顎顔面部 CT 画像からの歯の自動抽出.日本放射線技術学会雑誌. 2010 Apr 20:66(4);343-52.

Declaration

1. All the images (clinical images) were processed under the patients' consent that they approve the use for image processing in this study.
2. All the institutional review board (IRB) of hospitals (medical institutions) where the processed images were acquired have approved of the clinical image providing.

Acknowledgments

I would like first and foremost acknowledge and extend my heartfelt gratitude to my supervisor, Professor Hayakawa Yoshihiko, for his patient guidance, vital encouragement, and generous assistance, all of which have been of inestimable worth to the completion of my thesis.

Among the last five years, Professor Hayakawa guided me into the world of medical image processing. I was recommended to read books and papers of related fields, what made me surefooted on my research. Prof. Hayakawa also attached importance to developing my scientific research ability. He encouraged me to attend not only domestic but also international technology symposiums. They broadened my horizon largely, and leaded me to understand the advanced research. I did poster or oral presentations on the symposiums to introduce my research to others of relative fields. Under his patient guidance, I succeed in publishing 3 academic papers as first author on international journals collected by SCI. His attitude towards life and work will give a profound impact on my later life. I am feeling honored to study under supervision of Prof. Hayakawa.

To promote the cooperation study with Hamburg University of Applied Sciences, Professor Hayakawa provided me two months' study in Germany (1 month of each time for twice) under the supervision of Professor Cornelia Kober who is an expert of biomedical engineering. I learned much from the research of Prof. Kober, especially about the 3D visualization. I want to send my special thanks to Professor Cornelia Kober, faculty of life science, Hamburg University of Applied Sciences.

Next, I want to express my thankfulness to Hokkaido University Cooperative Pioneer Development System, Hokkaido University. They provided me the internship opportunity for three months (from Dec. 2012 to Mar. 2013) in

Yokohama Research Laboratory, Hitachi, Ltd. I learned knowledge of embedded system and did some basic research on embedded software development there.

The last but not least, my thanks would also go to my beloved parents for their boundless love and whole-hearted support over all these past years.